COMPUTATIONAL MODELING OF CONTROLLED CORTICAL IMPACT IN A MOUSE

by

Vishwas Mathur

A thesis submitted to the faculty of
The University of Utah
in partial fulfillment of the requirements for the degree of

Master of Science

Department of Mechanical Engineering

The University of Utah

December 2010

The University of Utah Graduate School

STATEMENT OF THESIS APPROVAL

The thesis of [redacted]

has been approved by the following supervisory committee members:

[redacted], Chair — 10/20/2010
Date Approved

[redacted], Member — 10/20/2010
Date Approved

[redacted], Member — 10/20/2010
Date Approved

and by [redacted], Chair of

the Department of Mechanical [redacted]

and by Charles A. Wight, Dean of the Graduate School.

ABSTRACT

Thresholds for primary vascular injury have not been well-defined. Various animal experimental models are available to study different types of injury and their severity, but quantifying the tissue deformations that produce the injuries is difficult. This project aims at developing a finite element (FE) model of controlled cortical impact (CCI) in a mouse in order to quantify brain deformations associated with the resulting contusion. The predicted deformations will be used to study the correlation between the mechanical responses and the experimental injuries. The model for this study was built by digitizing coronal section images of a mouse brain taken from an online database. The resulting model includes a total of 426,447 brick and shell elements to represent the brain, skull, impactor and the meninges. A contact algorithm was used to model interactions between the mouse brain and the impactor. Impact velocity and depth were governed by a prescribed displacement with respect to time for the impactor. The influence of these loading conditions, along with that of impactor size and shape and craniotomy size, were examined. The significance of mesh density, element integration schemes and contact algorithm was also examined. Not surprisingly, predicted peak mechanical responses in all the parameter studies conducted were localized in and around the region of the impact. Impactor shape and impact depth were the leading factors influencing the mechanical responses.

CONTENTS

LIST OF FIGURES

LIST OF TABLES

ACKNOWLEDGEMENTS

First of all, I would like to thank my advisor Dr. Ken Monson, for his invaluable guidance throughout my research work. I am deeply honored for having Dr. Monson as my advisor. His constant support be it academically, financially, or morally is beyond compare. Hurdles are the integral part of any success and Dr. Monson's faith in me, and expertise in the field have always helped me overcome them. I am grateful to my committee members, Dr. K.L DeVries and Dr. Rebecca Brannon, for their valuable suggestions and guidance.

I would like to extend my gratitude towards all the wonderful co-workers and friends I have had at the Head Injury Biomechanics laboratory, University of Utah. I would like to thank everyone at the University of Utah who has in one way or the other contributed towards my success. I am thankful to my lively and supportive roommates, Nikhil, Sadha, and Krishnaji, and friends around the valley for their help and support as and when required.

This list of acknowledgement is never complete before I thank two most important people in my life, my parents, thank you Mom and Dad. I would like to thank my entire family and the one above all of us, the omni present god for listening to my prayers and giving me strength and courage to face the challenges. Thank you GOD!!

CHAPTER 1

INTRODUCTION

A report by the Centers for Disease Control and Prevention (CDC) shows that out of 0.13 billion injuries each year in the United States nearly 5.5% are due to traumatic brain injury (TBI), occurring when an external force causes damage to the brain [5]. TBI accounts for 4.8% of all injuries seen in emergency department visits, 15% of all hospitalizations and 30.5% of all injury related deaths in the United States [5]. There was an increase of nearly 20% in injuries resulting from TBI in recent years with an approximate total medical cost of $60 billion [5] annually. Injuries resulting from TBI can be focal or diffuse and are classified as either primary injury occurring at the time of trauma or secondary injury occurring after trauma [6][7]. There are diverse causes of TBI with the majority of injuries reported due to falls, motor vehicle-accidents, struck by/against incidents and assaults. People in all age groups are affected by TBI, though the majority of cases reported are in children in the age group of 0-4 years and adults over 65 years [5].

Traumatic brain injuries have both short-term and long-term effects on individuals. TBIs may include cerebral contusion, subdural hemorrhage and other damage to blood vessels, axonal injury and brain swelling [6][7]. Even though TBI has devastating effects on humans, there is no way to prevent it completely. People with severe injuries due to TBI often need long-term rehabilitation to maximize their function and independence, while victims of mild TBI may also experience dramatic consequences [5].

1.1 Investigation of TBI

The mechanisms of brain injury need to be better understood to prevent these injuries, but reconstructing injury scenarios often becomes difficult due to lack of

data on human response. Animal models are a widely used alternative for replicating pathological conditions seen in human injury [8][9][4]. Human head finite element (FE) models have also been constructed to study mechanisms of TBI, but their usage is limited by a lack of in vivo data for their validation [10].

Head injuries are classified in multiple ways, including whether they are open or closed: Open head injuries occur when an object penetrates through the skull, while closed head injuries occur when an object does not pierce the skull [11]. Both of these types of injuries can be studied by using animal in vivo models. Such models can be classified by the type of injury they create, focal or diffuse, or by the type of loading they utilize, as, impact acceleration, inertial (nonimpact) acceleration and direct brain deformation/penetrating injury models [6][8][12].

1.1.1 Focal brain injury models

Focal brain injury is caused when the brain is hit by an object or struck against an object. These injuries are often penetrating, such as gunshot wounds. Cereberal contusions, extradural and subdural hemorrhages are some of the observed focal injuries [11]. Animal models that have been shown to reproduce these injuries are described below.

1.1.1.1 Direct brain deformation models

Direct brain deformation models are widely used in investigating focal TBI. While these models technically produce open head injuries, they are often used to study closed head injuries. Rodents are used widely as subjects for this study; however, a number of other species have also been used in the past. These types of deformation models use either a fluid or a rigid indenter to impact the brain [12][7]. Loading conditions in these models are well defined and are known to produce contusion, which largely prevails in TBI [8]. The two most frequently used deformation models are controlled cortical impact (CCI) and fluid percussion injury (FPI).

- Controlled cortical impact (CCI) model: This type of direct brain deformation model is used to create a contusion injury. The CCI model initiates brain injury by impacting the brain with a piston driven electrically or by a pneu-

matic cylinder as shown in Figure 1.1 [1]. Anesthetized rats or mice are fixed in position with a stereotaxic frame (Figure 1.1) and a small craniotomy is performed on the skull to impact the dura directly. The CCI model produces primarily focal injuries and is widely used to study TBI because it allows better control of loading parameters (like the velocity, the depth and the time) than other models [11][12][13].

CCI injuries have been performed on a number of species; however, injuries using CCI were first reported on ferrets [13]. Using ferrets for a wide range of deformation ranging from 2.5 - 4.5 mm, damage to the vasculature, including subdural hematoma and cortical contusion, was reported [13]. Depending on the injury severity, contusion and acute neurological deficits have been reported in rats. Moderate to severe injuries in rats include intraparenchymal hemorrhage and axonal injury [14]. Since in a CCI model, the loading parameters and the injury severity are better controlled, it can be helpful in studying various injuries seen in human TBI like subdural heamatoma, axonal injury, contusion, blood-brain barrier(BBB) dysfunction and coma [11]. Impact velocity and depth are known to govern injuries resulting from CCI [15]. These models are sometimes called contusion or rigid impactor models [15].

- Fluid percussion injury (FPI) model: Another widely used animal model of TBI is fluid percussion injury. As shown in Figure 1.2, a pressure pulse is applied to the dura, to produce the injuries [15]. As with CCI, contusions and subarachnoid hemorrhage have been observed at the site of impact, but some level of diffuse injury has also been observed. The pressure pulse most commonly applied at one of two sites: midline or lateral; lateral FPI are known to produce both focal and diffuse injuries [15]. Severe FPI has been shown to damage the brain stem [14].

1.1.1.2 Weight drop model

The weight drop model generally uses rodents as the subjects of investigation to produce closed head injuries. This model induces brain injury by using the force

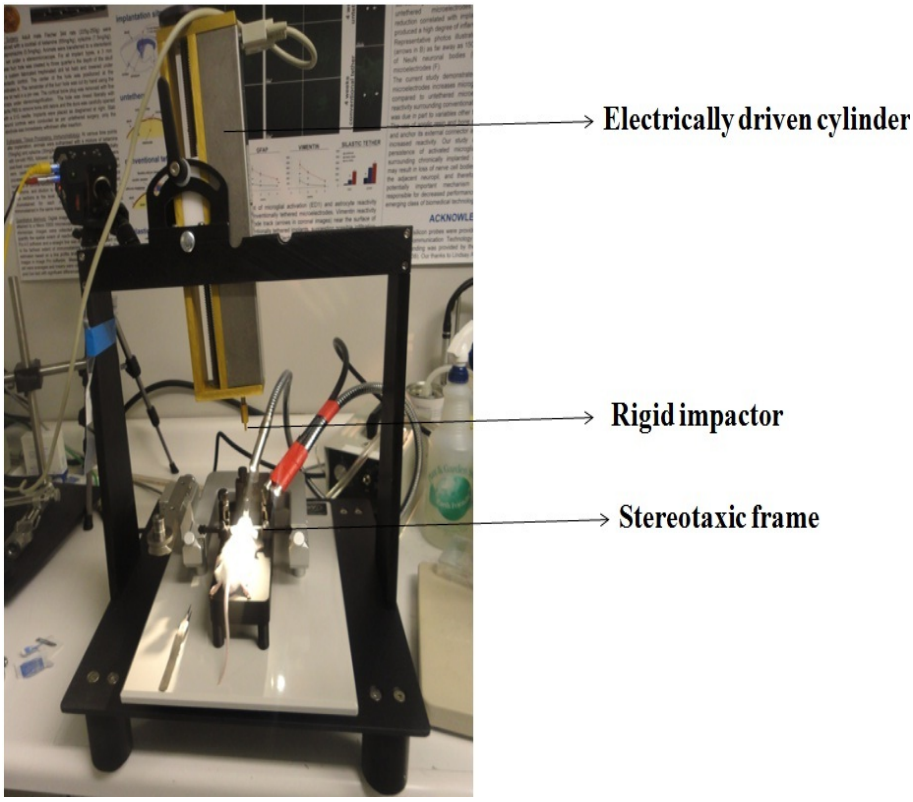

Figure 1.1. Controlled cortical impact device

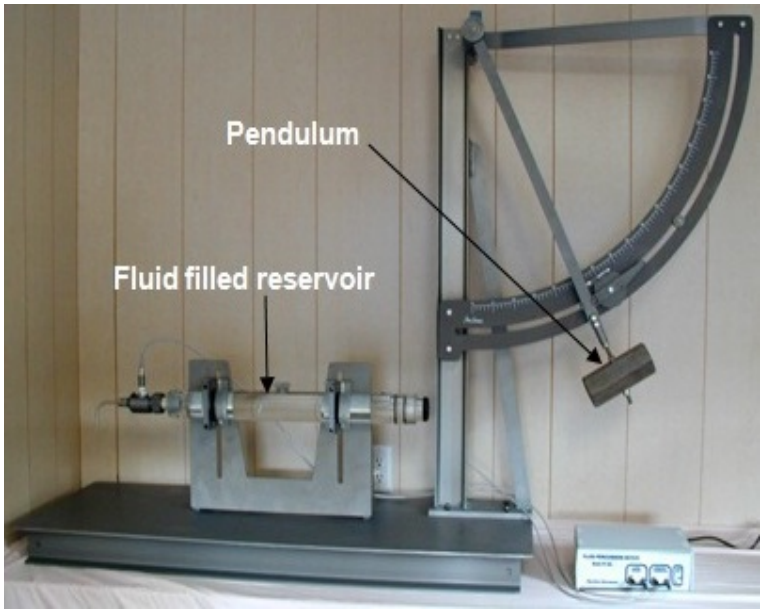

Figure 1.2. Fluid percussion injury device [1].

of a free-falling, guided weight. The heads of anesthetized rats or mice are exposed to these weight drops by positioning them at the bottom of the weight drop guide. Severity of the injury depends largely on the mass of the weight drop and height from which it falls [11]. The usage of this model is limited, however, because there is a possibility of skull fracture upon impact and a chance of a second impact by the weight after rebounding from the skull. Using this model over a range of severities, concussion, cortical cell loss and contusions have been observed [16][17].

1.1.2 Diffuse brain injury models

Diffuse, also known as multifocal injuries, are those that occur from widespread tissue distortion or shearing, associated with the inertial forces present at the moment of injury [11]. Diffuse injuries include traumatic axonal injury (TAI), and widespread micro-hemorrhage and commonly result from severe rotational accelerations present in many vehicle accidents and falls. A brief description of the two most commonly used models to study these injuries is provided below.

1.1.2.1 Impact acceleration model

The impact acceleration model (also known as the Marmarou model) is used mainly to study closed head injuries by producing TAI without any penetration through the skull. The loading mechanism in this case is identical to the weight drop model already described, but a steel plate (as shown in Figure 1.3) is glued to the vertex of the skull to protect against skull fracture [2]. This plate distributes loads widely over the skull. Prior to the impact, the animal's head is placed unrestrained on a foam block to allow some motion after the impact. A wide range of injuries have been studied using this model. Depending on the level of severity utilized, coma, axonal swelling and subarachnoid hemorrhage have been reported [2]. Apart from rodents, primates, cats, sheep and pigs are some of the other subjects used in this type of model [12].

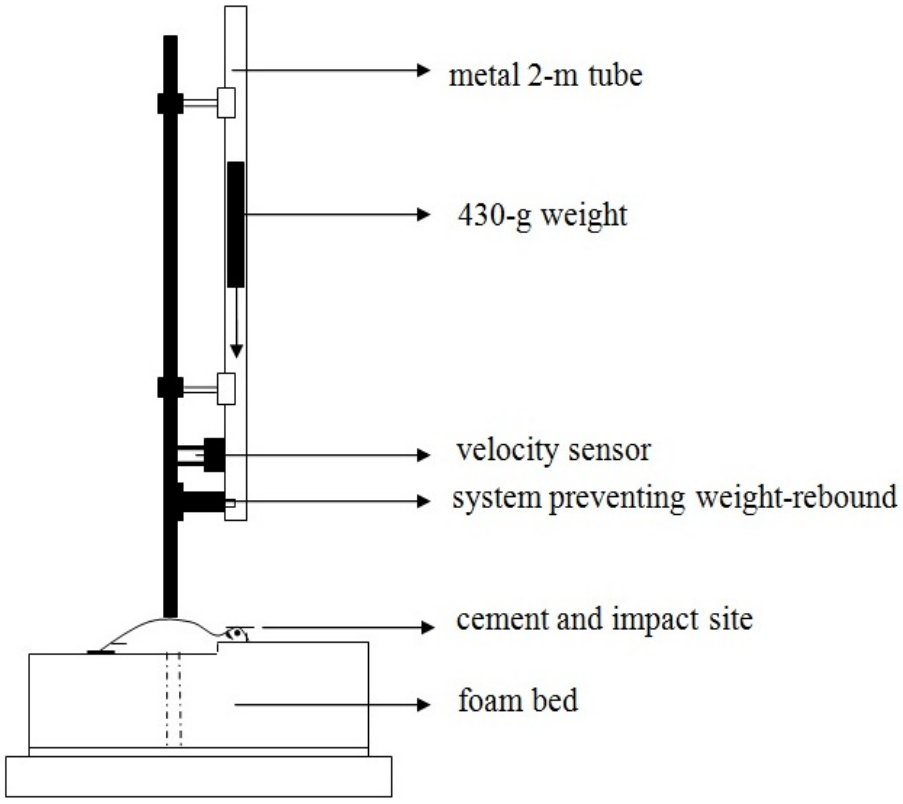

Figure 1.3. Impact acceleration model [2].

1.1.2.2 Inertial (nonimpact) acceleration models

Inertial acceleration models induce injury by acceleration of the head without any impact. Rapid rotation of the head is believed to be the major cause of diffuse brain injury [11]. These models are distinguished from head impact models by the relative absence of skull fractures in them. Inertial injury models with the non-human primates as subjects were utilized by Ommaya and Gennarelli in 1970s. More recently, mini-pigs have been used due to their relatively large brain-to-body mass ratio. According to the literature, injuries are produced by rigidly attaching the anesthetized animal's head to a fixture that is rapidly rotated over a defined angle for a very short time. The resulting rotational acceleration is biphasic, often having a relatively long-term acceleration phase followed by short deceleration phase. Experiments using this model have regularly reported neuronal loss, damage to hippocampal structures, acute subdural hematoma, coma and axonal injury in almost every study [18].

1.2 Review of Finite Element (FE) Models in Rodents

While the described experimental models are valuable for studying the relationship between loading parameters, injury type and severity, the associated brain deformations cannot be experimentally measured. Computational (often using the finite element (FE) method) models can be constructed to predict the mechanical responses of the brain to mechanical loading, allowing correlation with experimental injuries. Rodents are the most widely used subjects for investigation of TBI due to their ease of comparability with human data [14] and their small size and low cost [10]. To date, very few rodent FE models have been developed for the study of TBI.

A two-dimensional FE model of a rat brain built by Pena and group was the first FE model of CCI simulating the traumatic loading and its relation to the mechanical variables like tissue displacement, mean stress and shear stress [19]. This 2D FE model, due to the uncertainty in the tissue elasticity, was simulated using three different Young's modulus (E) values. Results from their model showed that regional elastic properties are important in studying the specific injuries in TBI.

A 3D FE model of a rat brain was constructed to study the influence of age on the stress and the strain distributions due to closed head CCI [20]. FE models of both neonatal and mature rat brains for closed head impacts were built, and as expected the results showed that neonatal brains develop larger peak stresses and strains than mature brains for the identical cortical displacements. However, neither of the above described models were validated against experimental data.

An FE model of cerebral contusion was developed to define thresholds for mechanical injury to the blood-brain barrier (BBB) in dynamic cortical deformations (DCD) produced with a vacuum pulse to the exposed dura [21]. This model predicted maximum principal logarithmic strain, principal stress and maximum von mises stress; however, maximum principal logarithmic strain was reported as the better predictor of BBB dysfunction. This FE model was validated by comparing the displacement of surface nodes in the simulation to the mean peak cortical displacement measured experimentally.

Recently, an FE model of a rat brain including distinct anatomical features and material properties was built at Wayne State University [4]. This model is the first FE model of CCI in a rat, which accounted for all the major components of a rat head and was simulated over a range of loading conditions taken from experiments. This model was validated against the same dynamic cortical deformation data Shreiber et al. [21] used above and was used to predict strain and the strain rate responses associated with CCI experiments. A set of simulations were run, to study the influence of mechanical parameters like impactor depth and velocity, and shape of impactor on the strain and the strain rate responses [22]. This model was also used to study the intracranial responses within cortical and subcortical layers where neuronal injury most commonly occurs [23].

1.3 Objective

The vast number of computational and loading parameters available are expected to make correlation between the computational and experimental results of different labs difficult to study. Computational models more closely relating to the experimental study being conducted are needed to study correlation of results. The objective of this research was to build a 3D FE model of CCI in a mouse in order to predict the associated cerebral deformations. The predicted responses can then be compared with experimentally observed injuries in our lab to study correlation between injury and predicted deformations.

Subsequent chapters of this thesis present in detail:

- Construction of an anatomically well-defined mouse brain FE model.
- Methods involved in simulating CCI in a mouse computationally, for identifying the mechanical responses like the strain, the strain rate and the stress.
- Influence of the impactor shape and size on the predicted mechanical responses by the FE model.
- Comparison of results between the realistic and the idealized model of a mouse brain.

- Effect of computational parameters (like contact interactions and mesh density) on the models outcome.

CHAPTER 2

METHODS

The construction of the FE model and the material models used are presented in this chapter. A detailed list of parameter studies and the verification tests conducted are explained. The validation of the model using hertzian contact theory is also presented in this chapter.

2.1 Mouse Brain Geometry

Any FE model requires an accurate and a well-defined geometry. To our knowledge, an FE model of mice has not been previously constructed. The model for this analysis was developed by digitizing a total of 37 coronal section images (Figure 2.1) of a 51 day old C57BL/6J male mouse taken from an online database called The Mouse Brain Library, a database consisting of high-resolution images of brains from different genetically characterized strains of mice [3]. The contour of the coronal section images were digitized using Vision Assistant (National Instruments). The digitized coronal plane data of all the coronal section images was imported into SolidWorks, using the XYZ curves option available in the software. The coronal section data of each image were positioned based on their distance from bregma, available in the mouse brain atlas [3]. These coronal plane data were represented as curves in the software (Figure 2.2), which were later joined to represent a 3D model using the LOFTED BOSS/BASE option available in SolidWorks. The constructed 3D model provided a reasonable approximation of the external features of the mouse brain as shown in Figure 2.3. Brain tissue was modeled as homogeneous without any distinct layers for hippocampus, thalamus, etc., as this research is focused primarily on knowing the mechanical responses of the brain tissue mostly in the cortex, in the region of the impact.

Figure 2.1. Representative coronal section images of mouse brain [3].

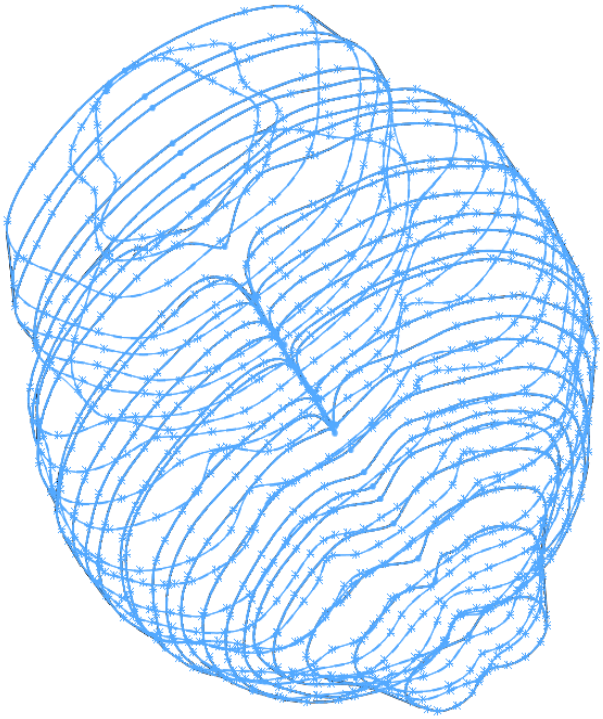

Figure 2.2. Curves depicting the coronal sections digitized for constructing 3D model.

2.2 FE Model of the Mouse Brain

The 3D model of the mouse brain, constructed using SolidWorks, was imported into Hypermesh 10.0 (Altair Engineering, Troy, MI) for mesh generation and other preprocessing. The brain tissue was meshed using brick (eight-node hexahedral) elements (Figure 2.4) and a total of 235,437 elements were used to represent it. In CCI experiments, impacts are directly to the exposed dura (via a small craniotomy) and not to the brain. Therefore, in order to model the meninges (dura, pia and

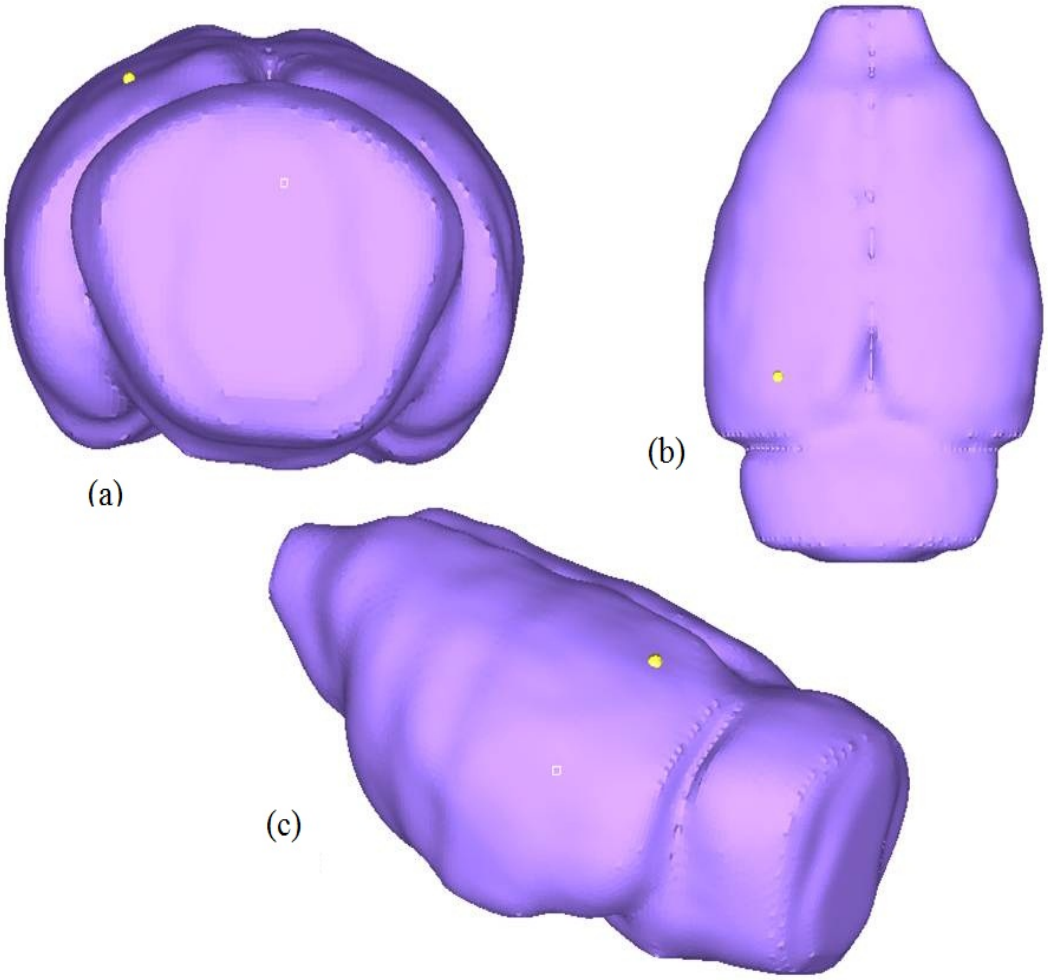

Figure 2.3. Reconstructed mouse brain geometry (a) Front, (b) top, and (c) isometric views.

arachnoid) of the mouse head, two separate layers of shell (four node quadrilateral) elements were generated above the brain surface. Pia and arachnoid layers were modeled together as one layer of shell elements on the outer surface of the brain tissue. Another layer of shell elements above the pia-arachnoid layer was created to represent the dura. The pia-arachnoid complex was generated by using the FACES option available in Hypermesh, while the dura layer was generated by duplicating the pia-arachnoid elements and offsetting them to a distance above the pia-arachnoid, such that the thickness of the layers was accounted for. A very small gap of less than half the thickness of the dura (0.01 mm) was introduced between the dura and the

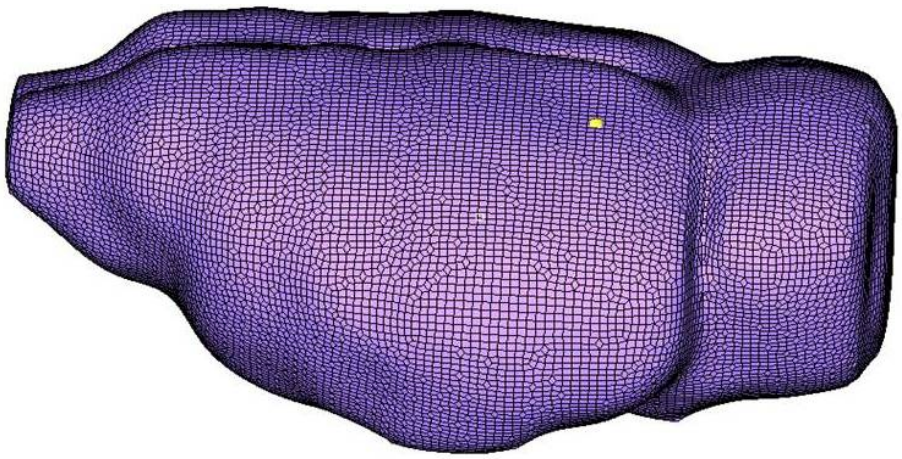

Figure 2.4. Brain tissue mesh

pia-arachnoid to account for the compression and the expansion of the brain tissue (incompressible material), within the boundary of the skull during the impact.

A single layer of brick elements above the dura was created to represent the skull. The impactor was modeled in SolidWorks with a hemispherical impactor tip (as seen in the experimental setup) and was meshed with brick elements. The dimensions of this impactor were taken from the electrical CCI device in our laboratory (obtained from Custom Design and Fabrication, Department of Radiology, VCU Medical Center). In total, the FE model was composed of 426,447 elements: two layers of 28,814 shell elements, representing the dura and the pia-arachnoid complex; 27,982 brick elements for the skull; 235,437 elements for the brain tissue; and another 105,400 brick elements for the rigid impactor. All the elements maintained a reasonable aspect ratio (<3), Jacobian (>0.7) and warpage angle (<20). The brain tissue was meshed with an element size of 117 μm. Figure 2.5 shows the meshed model including all the components. A hole (as shown in Figure 2.5) was created on the skull by removing the elements in the region where the impactor would otherwise make contact with them.

The LS-DYNA (LSTC, Livermore, CA) explicit solver was used to perform the dynamic analysis required for a CCI procedure. Contact algorithms were used to define interactions between the dura and the impactor as well as between the skull and the meninges. The skull which was modeled as rigid in CCI simulations serve

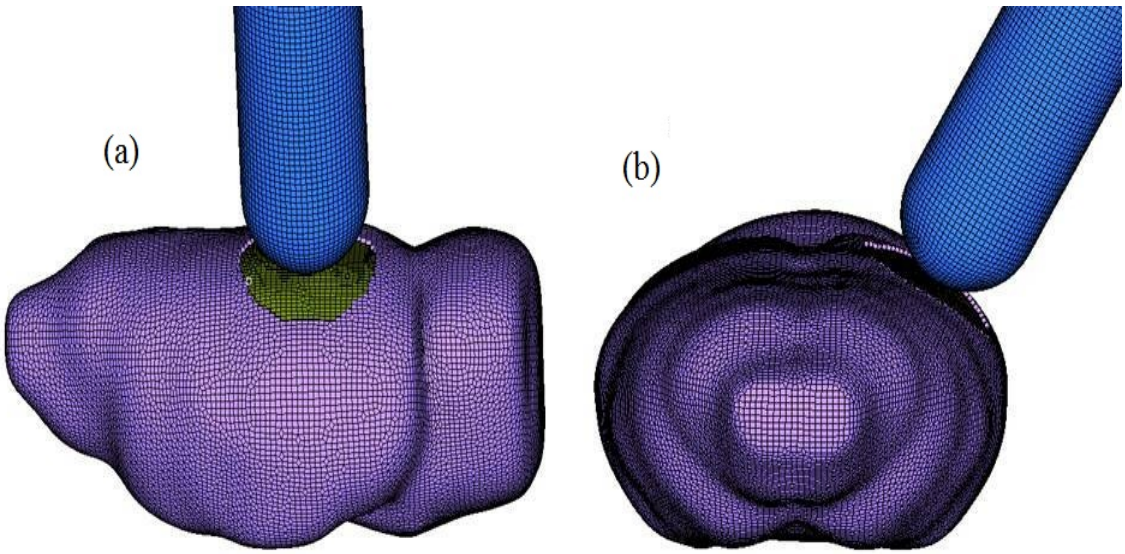

Figure 2.5. Model mesh with the hole depicting craniotomy

as the boundary for the meninges and the brain tissue. In total, three contact interactions were established to represent the mouse head and its interaction with the impactor. One contact interaction was set between the dura and the pia-arachnoid which essentially represented the interaction between the meninges and the brain tissue. In reality, the pia and arachnoid layers are separated by subarachnoid space, but in this study these layers were modeled as a single layer, following the same approach as Mao et al. adopted for their study [4]. The layer representing the pia-arachnoid complex shared common nodes with the top surface of the brain, so no contact interaction was defined between them. Two other contact interactions, one between the skull and the dura and another one between the impactor and the dura, were also defined.

All contact interactions used the CONTACT AUTOMATIC SURFACE TO SURFACE algorithm available in LS-DYNA. In all CCI simulations, the skull was held stationary, while the underlying tissue was allowed to move freely within the skull. The skull was held stationary by constraining all degrees of freedom of one of its node. The rigid impactor was similarly fixed in all directions except that of its defined motion.

2.3 Material Models

A linear viscoelastic material model previously used in the computational studies in rats was used to define the material properties for the brain tissue. In reality, the brain tissue is anisotropic and inhomogeneous due to distinct material properties of grey and white matter, as well as differences between various cerebral structures; it is also commonly considered to be incompressible due to its high water content [24]. In the presented simplified model, however, anisotropy and inhomogeneity were not considered, and all brain tissue was modeled as isotropic, homogeneous and incompressible material. The viscoelastic expression used to define the brain tissue is given in Equation 2.1 and the material constants for this study, listed in Table 2.1 were taken from the literature [4], with all brain tissue assigned properties of grey matter, as the cortical surface, which are of greatest interest in our study, are comprised of grey matter.

$$G(t) = G_\infty + (G_0 - G_\infty)e^{-\beta t} \tag{2.1}$$

where,
G_∞ is the long term shear modulus
G_0 is the short term shear modulus
β is the decay constant.

The meninges (the dura and the pia-arachnoid) were modeled as elastic, and their material constants are listed in Table 2.1. Both the skull and the impactor were modeled as rigid with material properties of steel: Elastic modulus = 200 GPa, Poissons ratio = 0.45 and Density= 7850 Kg/m^3. The dura and the pia-arachanoid layers modeled as shell elements were assigned a thickness of 20 and 15 μm, respectively taken from the literature [10]. This research work was focussed on the model framework and therefore validity of the material models used were given lesser importance.

Table 2.1. Material properties of the mouse brain and the meninges [4]

Material Properties		
Mouse Brain	Density	1040 Kg/m^3
	Bulk Modulus	2.1 GPa
	Long Term Shear Modulus	0.510 kPa
	Short Term Shear Modulus	1.720 kPa
	Decay Constant	20 ms
Dura	Density	1130 Kg/m^3
	Elastic Modulus	31.5 MPa
	Poissons Ratio	0.45
Pia/arachanoid	Density	1130 Kg/m^3
	Elastic Modulus	12.5 MPa
	Poissons Ratio	0.45

2.4 Idealized Model

An ellipsoid, as shown in Figure 2.6, was initially used to represent the idealized mouse brain. The meninges and contact interactions were set in a similar fashion to the realistic model. The idealized model was built in order to better understand the computational intricacies involved in simulating CCI. Therefore, this model was simulated over a range of loading conditions and computational parameters to understand the role of each parameter. This idealized model was later simulated, under the same baseline material properties and loading conditions utilized in the realistic mouse brain model, to compare the results of both models. Although mechanical responses obtained from FE simulations clearly depend on model geometry, the models were compared to obtain the similarities between the two.

2.5 Model Application

The realistic model, described in the previous sections, was also simulated under various loading conditions. The resulting strain, strain-rate and stress responses were evaluated both spatially and temporally, to study the correlation between these responses and experimental predicted injuries.

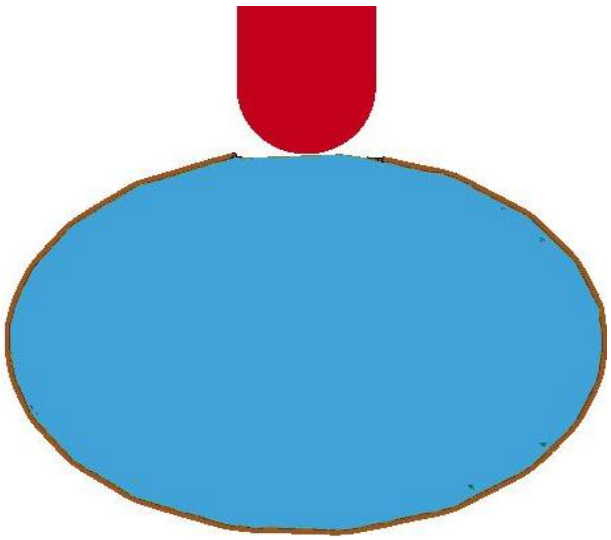

Figure 2.6. The idealized model of CCI.

2.5.1 Loading conditions

In all simulations the impactor was positioned to be perpendicular to the surface of the dura. Velocities ranging from 2 m/s to 7 m/s and maximum indentation depths up to 1.05 mm were simulated. Stress and strain for both nodes and elements was output at every 0.01 ms.

2.5.1.1 Parameter study

This section deals with the baseline case simulations of the FE model. The first row in the Table 2.2 shows the baseline loading conditions for this study. In the baseline simulation, the impactor was centered at a distance of 0.2 mm posterior of the bregma and 3 mm lateral of the sagittal suture; however, the skull, the brain tissue, the pia-arachnoid and the dura, as shown in Figure 2.7, were rotated to an angle of 35°, such that the impactor is perpendicular to the surface of the dura. The impactor was modeled with a hemispherical tip and with a diameter of 3.05 mm to match our experimental set-up. The baseline simulation had an impact velocity of 4.7 m/s, while the depth of the penetration was 0.7 mm. The material parameters for the baseline case are listed in the Table 2.1. Four other cases, with the same baseline parameters, were simulated with various combinations of loading conditions (Table 2.2) to study the influence of depth and velocity on mechanical responses obtained.

Table 2.2. Parameter study

Case	Impact Velocity (m/s)	Impact Depth (mm)
Baseline	**4.7**	**0.7**
A	4.7	0.35
B	4.7	1.05
C	2.35	0.7
D	7.05	0.7

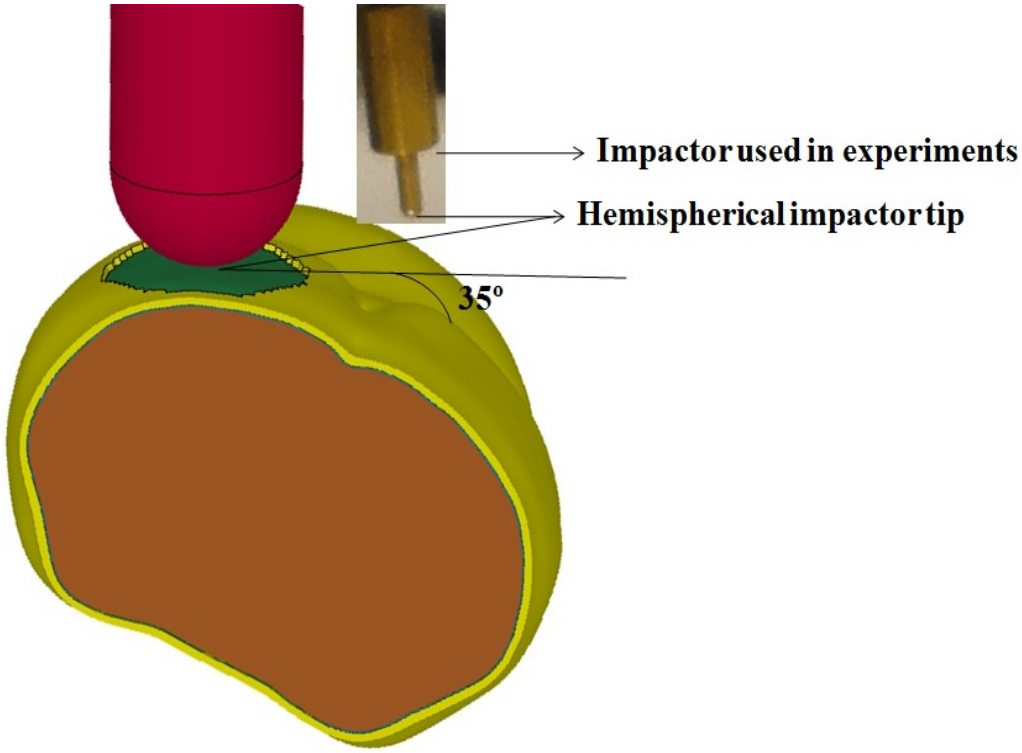

Figure 2.7. The baseline simulation of CCI, showing the impactor perpendicular to the surface of the dura.

2.5.1.2 Study of geometry and size of the impactor

The impactor used in the baseline simulations was modeled with a hemispherical tip; but the influence of other shapes and sizes were also explored. As shown in Figure 2.8, two impactors, one with sharp corners (at right angles) and a flat face and the other with rounded corners and a flat face, were modeled for this study. The fillet radius for the rounded corners (semiflat impactor) was taken as 0.5 mm, while the cylindrical diameter (3.05 mm) of both the impactors was the same as the hemispherical impactor used in our experimental set-up. Models utilizing each

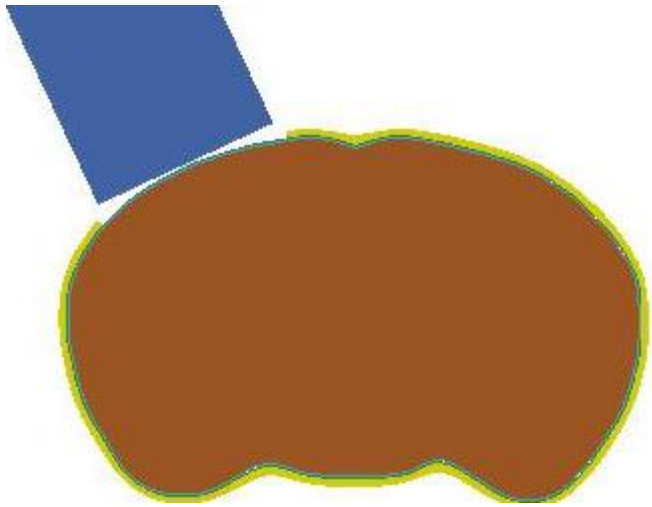

(a)

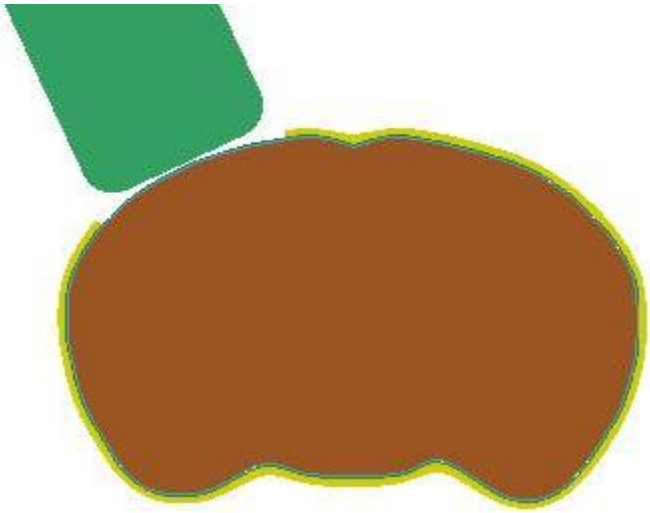

(b)

Figure 2.8. Impactor: (a) flat, and (b) semiflat tips.

of the impactor shapes were run, while all the other parameters were set same as the baseline case. Influence of the impactor size was also studied by running one additional baseline simulation with a hemispherical impactor tip of a larger diameter (5 mm), along with a larger craniotomy.

2.5.1.3 Mesh convergence

In all FE analyses, results are influenced by element size. To ensure convergence in the described model, different mesh densities were studied. Element sizes ranging from 100 to 400 μm were explored in the realistic model, but convergence was

also investigated in a model with idealized geometry. The idealized model for the convergence study was built by extruding the elements of a coronal section of the brain tissue from the realistic model (Figure 2.3). This coronal section was meshed with the element sizes shown in Table 2.3, while element size for the other layers (dura, impactor and skull) was kept constant. However, since the pia-arachnoid layer shared the outer surface nodes of the brain tissue, this layer was also re-meshed to match the nodes of the outer surface of the brain tissue. As shown in Table 2.3, the finest mesh explored led to an element size of 80 μm and 394,800 brick elements, while the coarse mesh had an element size of 200 μm and approximately 41,220 brick elements. Figure 2.9 shows the realistic and idealized models with different element sizes used for this study. All the simulations were run using baseline parameters and loading conditions.

2.5.1.4 Dwell time

Dwell time is generally incorporated in CCI experiments, which refers to holding the impactor at its maximum penetration depth for certain time period ($\sim$ 100 ms) before it is released back. To our knowledge, the influence of dwell time in CCI has not been previously examined. The reason for the use of dwell time in CCI is not clear, but it is expected to have some influence on injury outcome. In the baseline simulation a zero dwell time was set, however, to examine the effect of dwell time, two simulations (Table 2.4) were run using a 0.5 and 1 ms dwell time.

Table 2.3. Idealized model element sizes for mesh convergence study

Case No	Element Size (μm)	No. of Elements
1	200	41,220
2	140	81,872
3	120	170,600
4	110	222,033
5	100	315,840
6	80	394,800

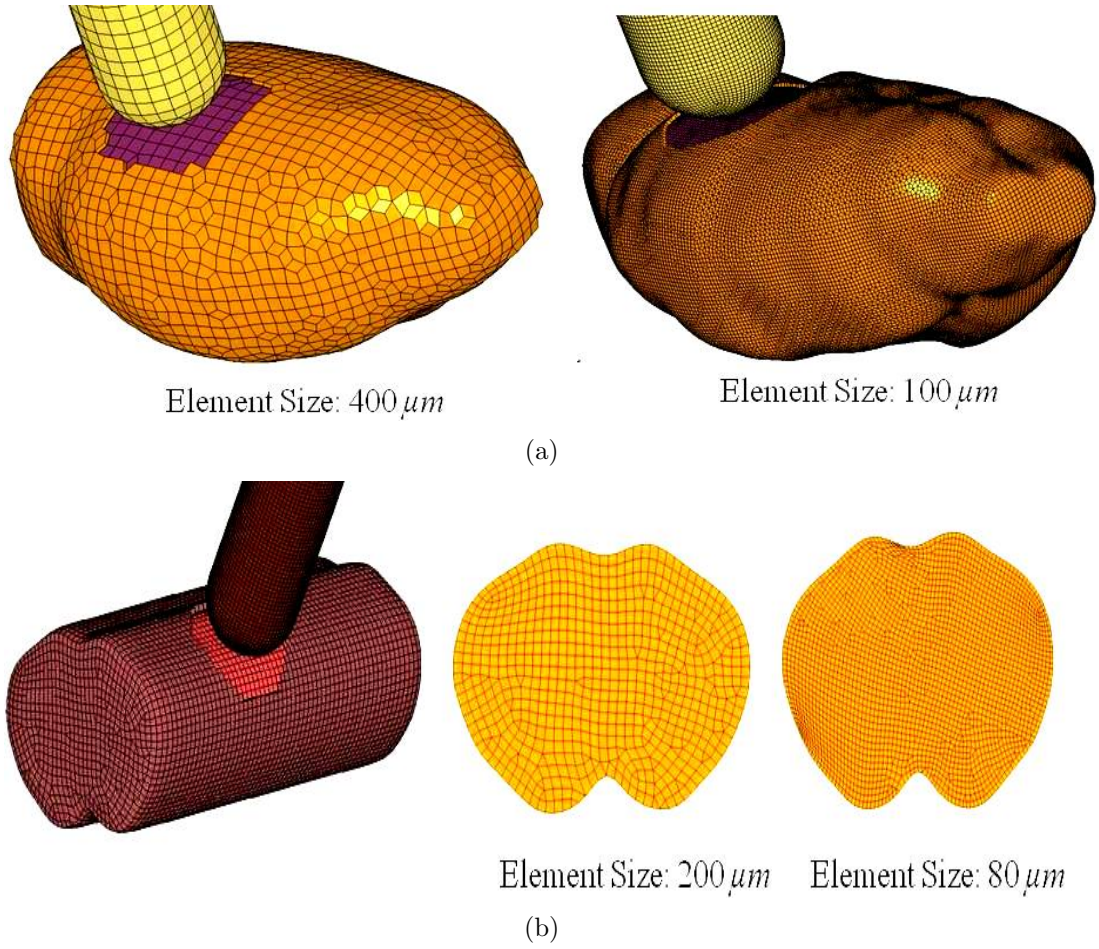

Figure 2.9. Mesh convergence study :(a) realistic model showing the largest and smallest element sizes explored; (b) idealized model for convergence study and corresponding coronal sections with largest and smallest element sizes explored.

2.5.1.5 Material parameter study

Material properties for this study, taken from the literature had different properties for different regions of the brain. However, this investigation was restricted to cortical surface, mainly at the site of impact and hence properties of the grey matter were used. To examine the influence of material properties on the mechanical responses, the decay constant, and the difference between the short and the long term shear modulus was varied as listed in Table 2.5. All simulations were run with an impact velocity of 4.7 m/s and 0.7 mm i.e the baseline loading conditions. In addition to the above simulations, a simulation with the brain tissue represented as an elastic material was simulated for the material model comparison.

Table 2.4. Dwell time study

Case	Impact Velocity (m/s)	Impact Depth (mm)	Dwell Time (ms)
A	4.7	0.7	0.5
B	4.7	0.7	1

Table 2.5. Material parameter study

Case	Short Term Shear Modulus, G_0 (kPa)	Long Term Shear Modulus, G_∞ (kPa)	Decay Constant, β (ms)	Impact Velocity (m/s)	Impact Depth (mm)
A	1.115	5.1	20	4.7	0.7
B	2.325	5.1	20	4.7	0.7
C	1.720	5.1	5	4.7	0.7
D	1.720	5.1	40	4.7	0.7

2.5.1.6 Site of the impact and craniotomy size

In all the above described simulations, the impactor was centered at a distance of 0.2 mm posterior of the bregma and 3 mm lateral of the sagittal suture, while the hole on the skull was created on the right hemisphere of the brain tissue. This study focussed on identifying the change in mechanical responses by changing the site of the impact and also by increasing the diameter of the hole on the skull. However, the material properties and the loading conditions were the same as the baseline simulations.

2.6 Model Verification

This FE model was constructed to simulate a phenomena for studying the brain injuries, which are difficult to measure visually and/or experimentally. Verification of this FE mouse brain model was focused on identifying whether the type of elements, the material models and other computational parameters used in CCI simulations were appropriate or not. Verification of the FE mouse brain model was done by constructing simple geometries like a membrane with shell elements, rectangular blocks with brick elements and in some cases single element models. To fully verify the FE mouse brain model, separate tests, each looking at different aspects of the model were conducted. In all of the verification testing, the model was simulated

over a wide range of loading conditions to understand the computational intricacies involved.

2.6.1 Shell element testing

Two layers of shell elements were wrapped around the brain tissue to represent the dura and pia-arachnoid in this FE analysis. These elements were assigned very soft material properties and, hence, verification testing was conducted by modelling two rectangular-shaped shell membranes with the thickness of the dura and the pia-arachnoid used in the model. The nodes on the edges of these shell membranes were constrained to all degrees of freedom. Two different tests were conducted- one with a single membrane of shell elements representing the dura and the other with two membranes representing both the dura and the pia-arachanoid. The impactor was positioned such that the impact was to the middle of the shell membrane, representing the dura in both the cases. These tests resulted in the deformation shown in Figure 2.10(a), with stress contours spreading approximately uniformly over the entire membrane. The maximum stress value was also observed at the time of the maximum penetration, as expected. Shell element verification testing showed no unexpected penetrations or distortion of elements, and all the elements maintained a good aspect ratio at various velocities.

2.6.2 Brick element testing

The brain tissue modeled using brick elements with a linear viscoelastic material model was tested using a rectangular block with two layers of shell elements on its outer surface to represent the dura and the pia-arachnoid. The rectangular block was first tested without the overlying shell elements. In this test, where the impact was to the rectangular block representing the brain tissue, showed stress and strain distribution uniformly over the block without any unwanted distortion of the elements. Next, two layers of shell elements above the brain tissue were incorporated in the model to represent the meninges and the impact was to the outer shell layer representing the dura. As observed in the first case this model also showed similar deformation patterns. Later on, one other layer of brick elements for the skull on the

outer surface of the dura was incorporated in the model. This represented CCI model on a simple geometry shown in Figure 2.10(b). The use of fully integrated elements to represent the dura and the pia-arachnoid resulted in termination of the simulations with a negative volume error for the given loading conditions of 0.7 mm depth and an impact velocity of 2.5 m/s. The lack of any space between the layers (the dura, the pia-arachnoid, the brain tissue and the skull) and the incompressibility of the materials could not accommodate the deformations with fully integrated elements and, therefore, terminated with severe distortion of elements. For the same loading conditions as the above, the use of single integration elements for the dura and pia-arachnoid behaved ideally for the simulation and have shown to be more robust than the fully integrated elements and hence were used. However, the brain tissue was modeled with single integration elements for all the tests. The stresses in the brick elements representing brain tissue in the above tests showed the maximum stress at the time when the impactor was at its maximum depth and then decreased over time as shown in Fig 2.10(c), but had a slow rate of decrease, which is expected due to the viscous nature of the material.

2.6.3 Single element testing

Single element testing was also performed to test, whether the material models used in the study were appropriate or not. The top four nodes of a single brick element (Figure 2.10(d)) were compressed to 20% of the elements length by assigning a prescribed displacement motion with respect to time (in the Z-direction), similar to motion of the impactor in CCI simulations. All three material models, representing the dura, the pia-arachnoid and the brain tissue, were tested using the single element test. The stress value predicted by all three material models matched the theoretically calculated stress values, thereby confirming that the material models used in this study were appropriate.

2.7 Model Validation

The FE model built for quantifying deformations associated with CCI is yet to be validated with experimental data. However, an analytical solution for finding the

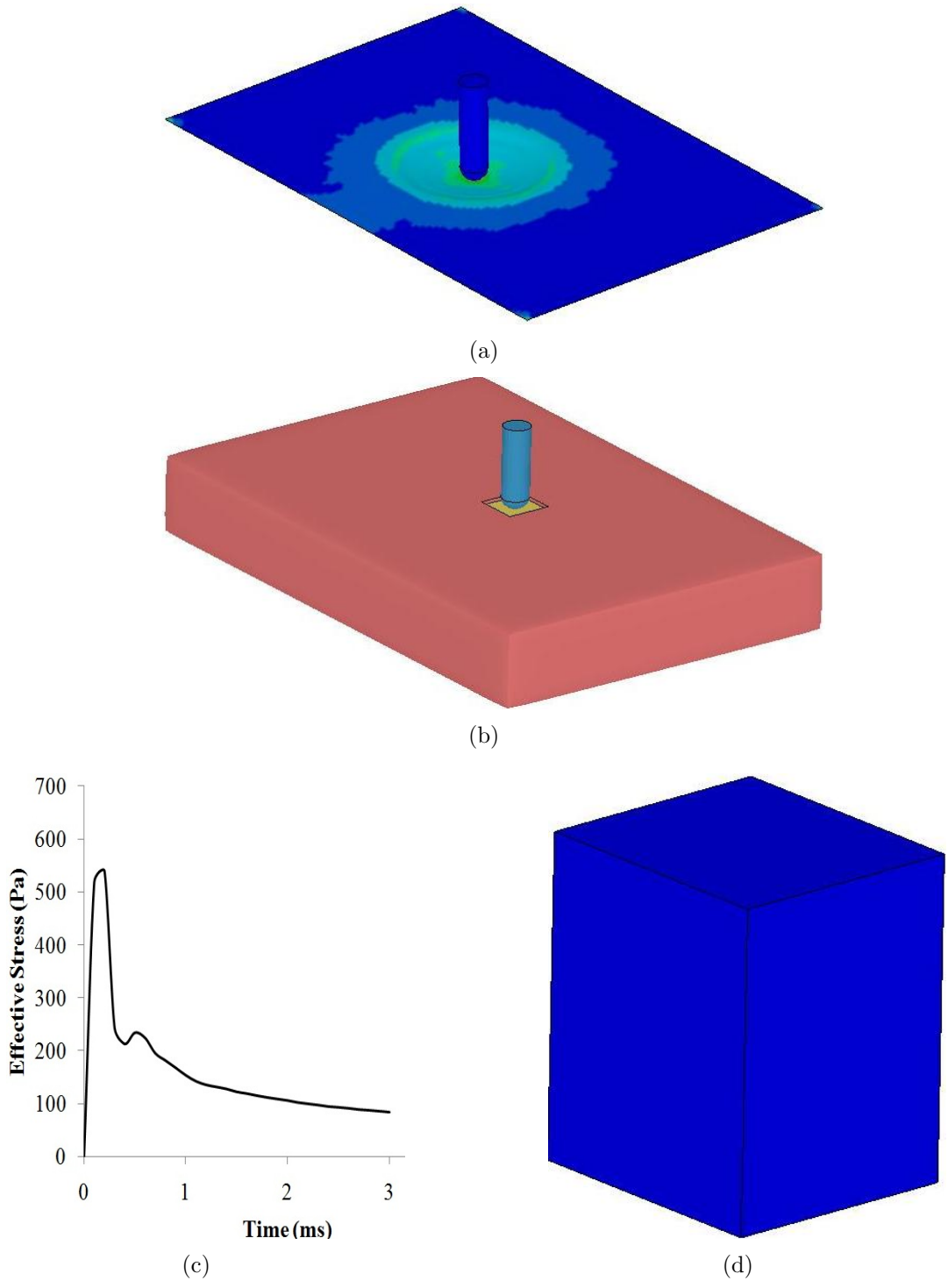

Figure 2.10. Verification test :(a) stress distribution contours from shell elements test (b) rectangular model representing CCI (c) rectangular block (brain tissue) stress plot over time (d) single element test.

stresses due to contact of two elastic solids, proposed by Hertz was used to validate the simplified 3D FE model [25]. Out of the various classical solutions proposed by Hertz for contact of solids with different geometrical surfaces, the expressions for calculating the contact stresses due to a rigid spherical indenter, indenting a flat surface were used in validating the simplified model shown in Figure 2.11. As the Hertz contact theory is applicable to elastic solids under very small strains, this simplified model was assigned the elastic material properties that of the dura and only small strains were simulated for comparison of results. The simplified model was built such that the contact area is much smaller compared to the dimensions of the model, and a very fine mesh refinement was generated in the area of the contact to accurately predict the results.

In validating the model, the same contact algorithm, between the rigid indenter and flat surface (rectangular block in this case), as in the realistic FE model was used. The expressions listed below were used in calculating the normal pressure distribution [25].

$$\frac{1}{E^*} = \left(\frac{1-\nu_1^2}{E_1}\right) + \left(\frac{1-\nu_2^2}{E_2}\right) \tag{2.2}$$

$$\frac{1}{R} = \frac{1}{R_1} + \frac{1}{R_2} \tag{2.3}$$

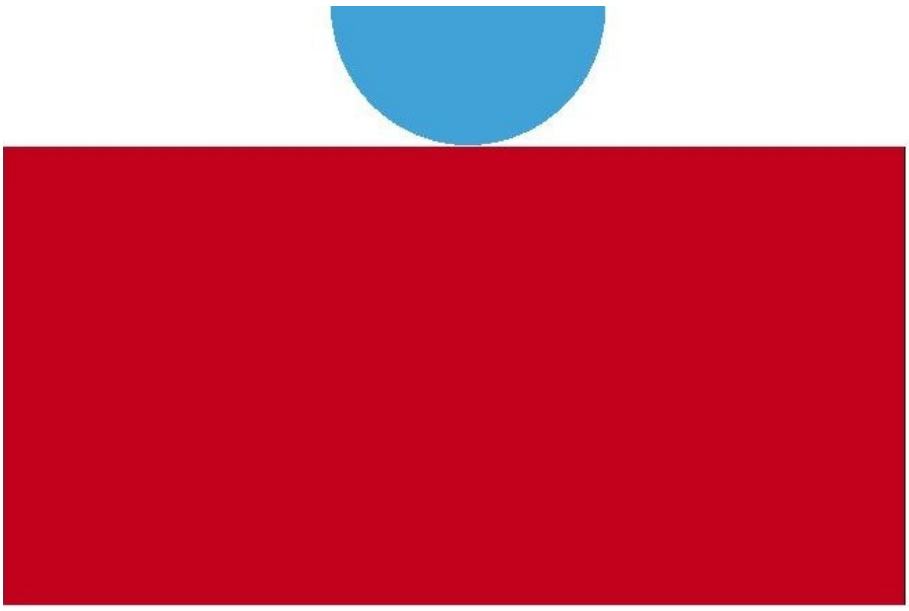

Figure 2.11. Simplified model for validation against Hertz analytical solution.

$$\delta = a^2 R \tag{2.4}$$

$$a = (\frac{3PR}{4E^*})^{\frac{1}{3}} \tag{2.5}$$

$$p_0 = \frac{3P}{2\pi a^2} \tag{2.6}$$

$$p = p_0(1 - (\frac{r}{a})^2)^{\frac{1}{2}} (r < a) \tag{2.7}$$

where,

E^* is the combined modulus of indenter and the flat surface

ν_1 is the poisson's ratio for indenter

E_1 is the elastic modulus for indenter

ν_2 is the poisson's ratio for flat surface

E_2 is the elastic modulus for flat surface

R is relative curvature of indenter and the flat surface

R_1 is radius of indenter

R_2 is radius of flat surface

δ is depth of penetration

a is contact radius

P is the total load compressing the solid

p_0 is maximum pressure

p is the normal pressure distribution proposed by Hertz

r is the distance.

The FE model predicted normal stresses were compared with the calculated normal pressure distribution for the validation. The contact radius and the maximum shear stress were also compared with the analytical solution. As the Hertz contact theory does not account for the velocity of the impact, three different velocities were simulated such that the contact force predicted by the FE model matches the theoretically calculated contact force. As expected, a decrease in the velocity resulted in a decrease in the contact force, and at a velocity of 0.5 m/s the FE model predicted contact force and the theoretically calculated contact force had a difference of less than 5 % between the two. As shown in Figure 2.12, the normal stresses on the surface of the contact are plotted against the ratio of distance over the contact radius

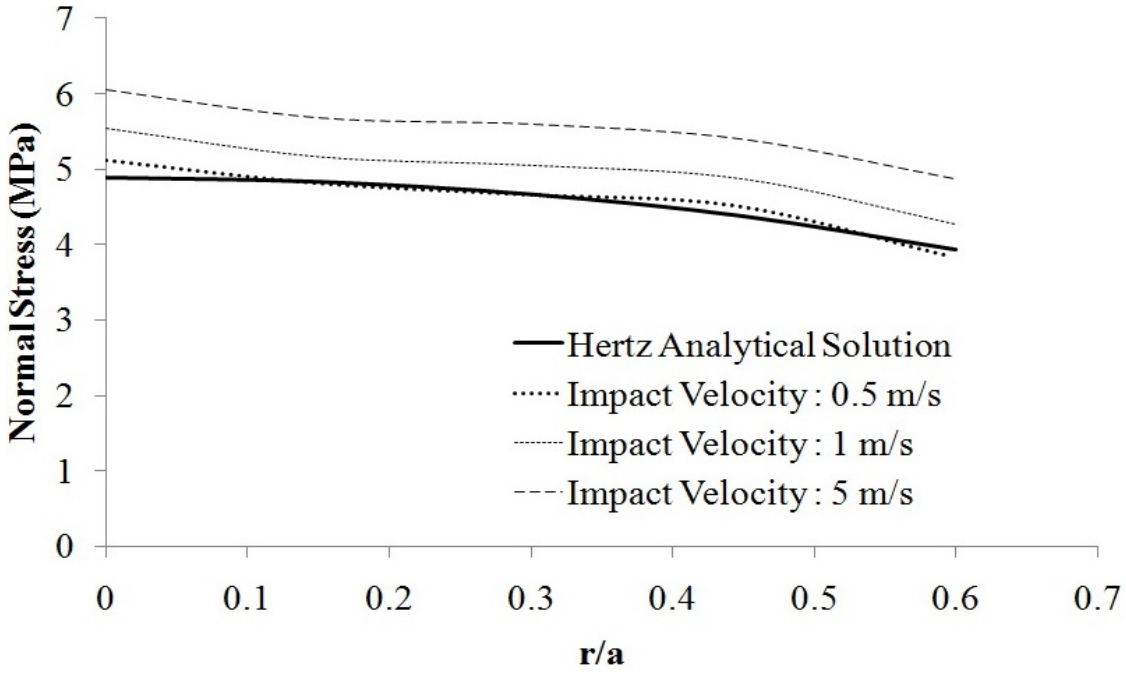

Figure 2.12. Plot of normal stress against the ratio of distance over the contact area.

(r/a). The normal stresses at a velocity of 0.5 m/s correlated with the theoretically calculated stresses. Moreover, the maximum shear stress value (1.58 MPa) predicted by FE model was also observed to be in agreement with the theoretically calculated value (1.51 MPa) with a percentage difference of 4.1 % between the two, and these stresses were observed below the surface of the impact (Figure 2.13) as proposed by Hertz. This 3D FE model results are in agreement with the Hertz analytical solution results, thereby validating the model.

2.8 FE Sensitivity Analysis

The influence of contact interactions and hourglass controls were also examined to avoid any undesirable results. In total, three contact interactions were defined in these simulations. An automatic algorithm was used because of its advantage in detecting penetration from either side of a surface. Unlike other contact algorithms, this algorithm is symmetric and hence the definition of the master and the slave segments is not of high importance. The algorithm uses a penalty method to determine contact

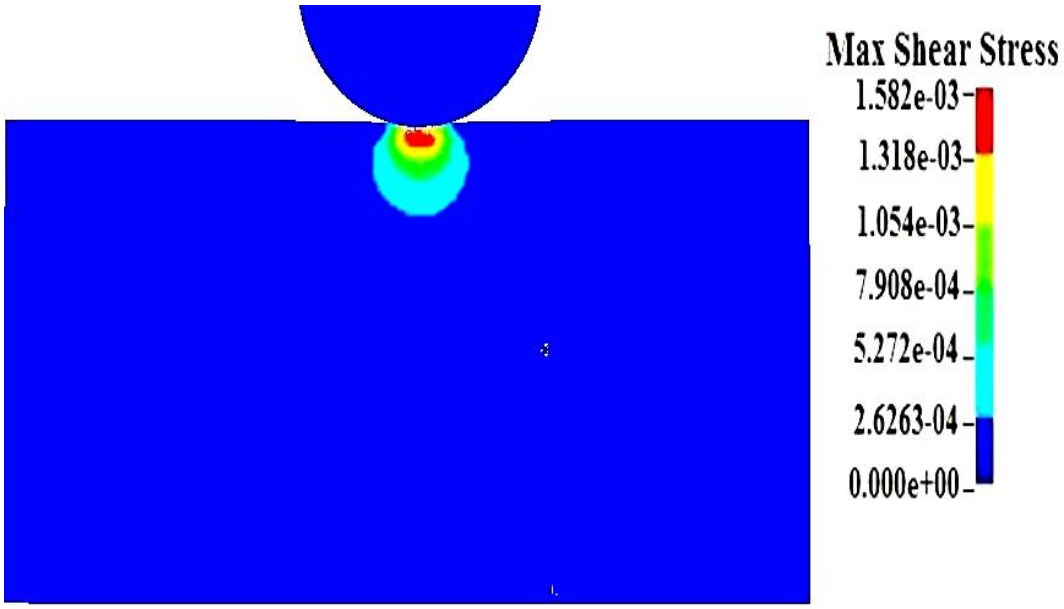

Figure 2.13. Shear stress distribution for the rectangular block showing the maximum shear stress below the surface of the impact.

stiffness and can be implemented by three formulations: standard, soft constraint and segment-based.

In this research, the surfaces in contact had very soft material properties with different material stiffness; simulations using three different formulations were run separately to choose the appropriate one. The standard formulation, which is intended for materials with approximately same stiffness [26], resulted in the failing of the contact with the penetration of impactor elements into the dura elements during impact. Both the soft constraint and the segment-based penalty formulations are termed to be suitable for dissimilar mesh densities and material stiffness. The segment-based formulation is similar to the soft constraint option, except for the parameters used to determine the contact stiffness and, like the soft constraint formulation, it also calculates an additional stiffness based on the time step. Use of the soft and segment-based formulations resulted in no penetrations, so penalty method algorithms with soft constraint and segment based formulations were implemented. Scaling down the global time step also eliminated contact penetrations. Therefore, a penalty formulation with a scaled down global time step was implemented in further

simulations. A coefficient of friction (μ) of 0.2 was defined between the contacting surfaces, based on the literature [4].

Hourglassing (HG), an undesirable zero energy mode, is known to occur in the reduced integration element formulations. These energy modes deform the elements in a zig-zag manner, and the occurrence of these deformations can invalidate results [27]. In the presented simulations, reduced integration element formulation (single integration elements) were used to reduce computational times. Literature, related to hourglassing demonstrates the need to suppress this energy to less than 5% of the total internal energy of the system. To control these energy modes, different viscous-based and stiffness-based hourglass controls were implemented with the reduced integration elements. The hourglass coefficient responsible for adding the viscous damping and/or artificial stiffness to control these modes was altered to study its influence. However, the default viscous-based HG control available in LS-DYNA was implemented over the stiffness based control due to the overly stiff behaviour of the model with the later. A similar observation about the overly stiff response of the model while using stiffness based HG controls was made by Takhounts et al. [28], in their work on developing the SIMon finite element head model. However, using the viscous HG controls did not decrease the high HG energy values recorded in the current model contrast to that reported by Mao et al. [4] with LS-Dyna Type 2 viscous HG control in their study of TBI using DCD and CCI simulations. Since neither mesh distortion nor any nonphysical deformations were observed in these simulations, the default HG control was used in all the CCI simulations reported. However, fully integrated elements does not encounter these energy modes, but are susceptible to element locking, as observed for shell elements in verification testing, and result in much higher computational times and hence were not used.

CHAPTER 3

RESULTS

This chapter presents the results for the CCI simulations described in the previous chapter (Section 2.5). All the simulations were run on an eight Dual-Core AMD Opteron (TM) 8220 processors machine with a RAM of 66 GB. Even with this computational power, average run time for these simulations was 25h, with a maximum of 60 h required to simulate the mesh convergence study with more than 300,000 elements. Figure 3.1 shows the impactor deforming the dura, which inturn deforms the brain tissue.

3.1 Results

3.1.1 Parameter study

3.1.1.1 Baseline results

Figure 3.2 shows the Green-Lagrange first principal strain distributions at three different regions in the brain tissue for the baseline case (penetration depth of 0.7 mm and impact velocity of 4.7 m/s). As expected, high strains were observed in and around the site of the impact; no significant increase in strain was observed in areas

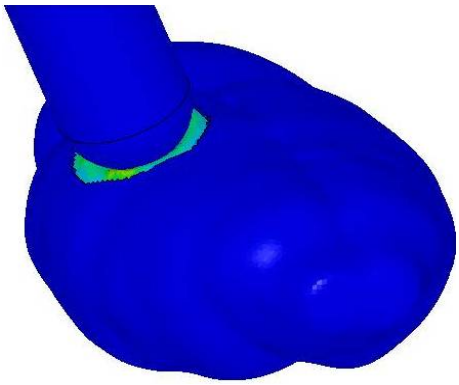

Figure 3.1. Deformation of the brain tissue in a CCI simulation

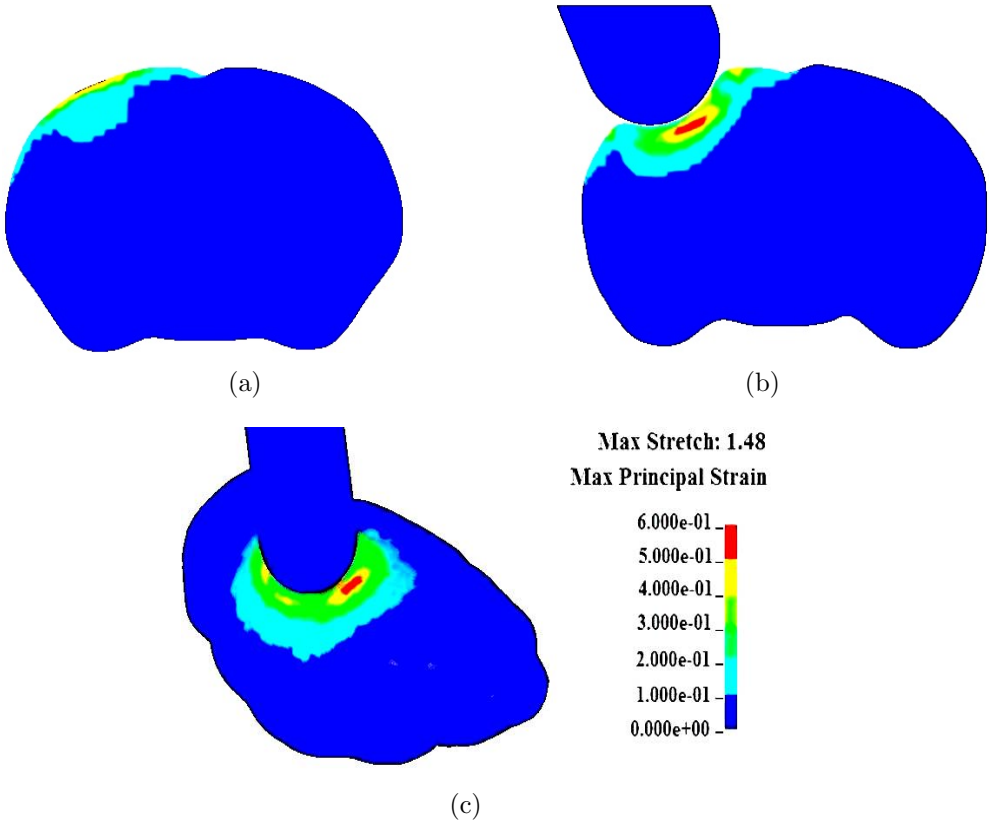

Figure 3.2. Green-Lagrange first principal strain in the brain, for a maximum depth of 0.7 mm: Coronal sections of the brain (a) adjacent to the site of impact and (b) at the center of the impact site, (c) isometric view showing strains around the impact site.

remote from the impact site (Figure 3.2(c)). As shown in Figure 3.2(b), the maximum strain was recorded below the impact surface at 0.15 ms, when the impactor was at its maximum depth. As a result of the impactor compressing the dura, high strains developed in the brain tissue, and these high strains traveled from the cortical layer into the deeper regions of the brain tissue (Figure 3.2(b)). However, these strains were released once the impactor was retracted back.

Figures 3.3 and 3.4 show the strain and the strain rate history averaged for six elements of the brain tissue outer surface at the center of the impact site. The strain plot shows a gradual increase in strain values, reaching a peak value of 0.22 at the time when the impactor was at its maximum penetration depth, and then a decrease once the impactor was retracted back. However, the maximum strain value

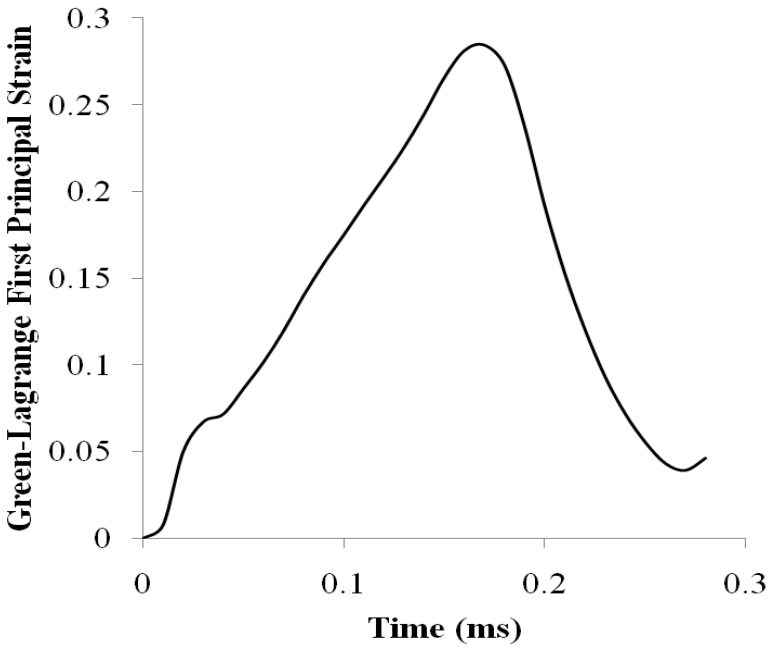

Figure 3.3. Green-Lagrange first principal strain plotted over time for the elements on the brain tissue at the center of the impact site.

of 0.67 (stretch (λ) = 1.52) was recorded in the brain tissue below the surface of the impact at the time when impactor was at its maximum depth. Unlike the strain plots, the maximum strain-rate value of 3.0 ms^{-1} was observed at the time when the impactor first contacted the surface of the dura. However, after a sudden initial change in strain-rate, the strain-rate plot does not show any large change for the time the impactor was deforming the dura. A rapid decrease in the strain-rate is observed when the impactor was retracted back, which suggests that the brain tissue is responding rapidly to the removal of impactor.

Figures 3.5 and 3.6 show the stress and the strain-rate distributions in the brain tissue for the baseline case at a maximum depth of 0.7 mm. The maximum stress was seen below the surface of the impact (Figure 3.5), similar to the strain distribution. Again, as expected no increase in the stress was observed in the areas remote from the site of the impact. However, the strain-rate distribution contours are different from both the stress and the strain distributions, showing maximum strain-rate in the region of the impact (Figure 3.6) and a high level of strain-rate distribution for a greater region in the brain tissue.

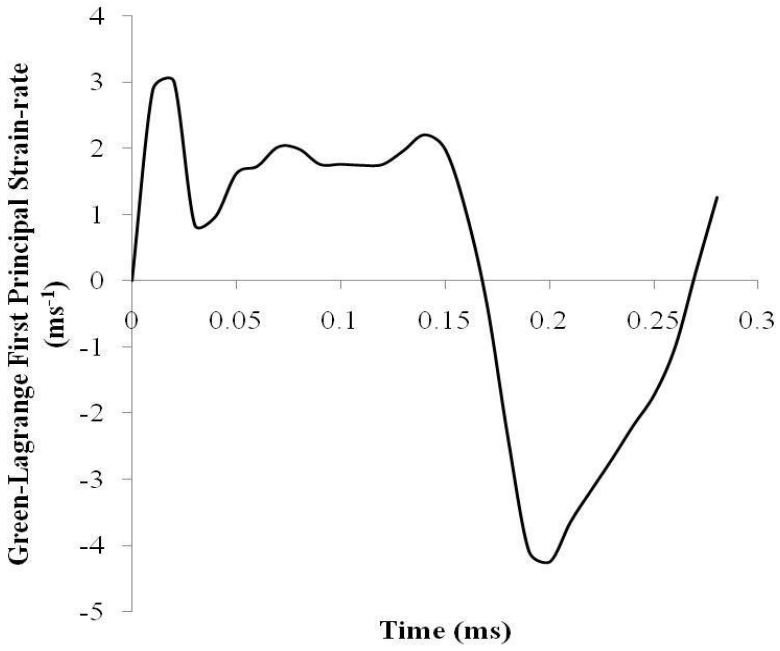

Figure 3.4. Green-Lagrange first principal strain-rate plotted over time for the elements on the brain tissue surface at the center of the impact site.

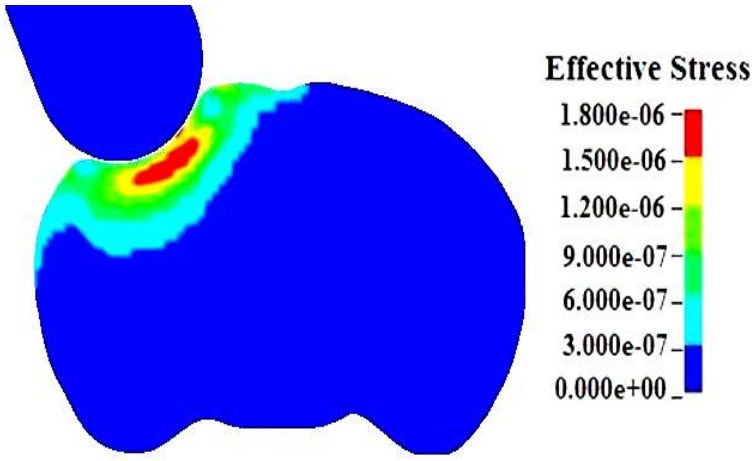

Figure 3.5. Effective stress distribution on a coronal section of the brain at the center of the impact site for a maximum depth of 0.7 mm. Units: GPa

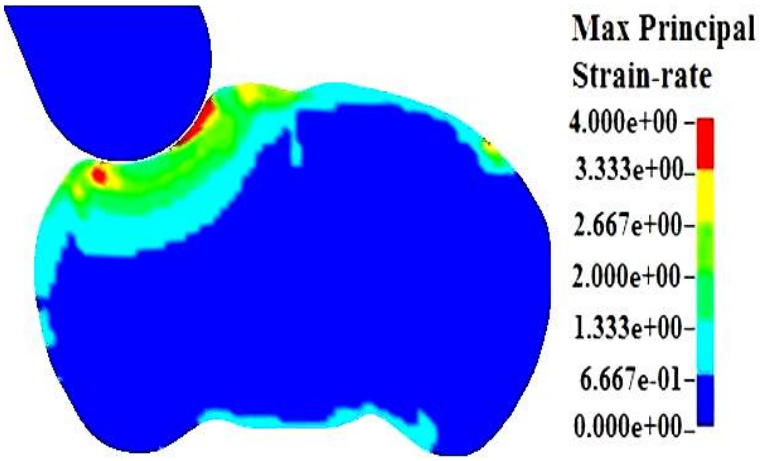

Figure 3.6. Logarithmic first principal strain-rate distribution on a coronal section of the brain at the center of the impact site for a maximum depth of 0.7 mm. Units: ms^{-1}

3.1.1.2 Influence of impact velocity and depth

To study the influence of velocity and depth on the mechanical response, four additional simulations in comparison to the baseline simulation were run. Figures 3.7, 3.8, and 3.9 show the strain, strain-rate, and stress distributions on the brain tissue for the simulations by varying the impact depth and the velocity, as listed in Table 2.2. As shown in Figure 3.7, changes in velocity and depth of impact produced large variation in the strain distributions compared to the baseline case. The maximum strain values for an impact depth of 1.05 mm were higher than the baseline case and these maximum strains were not only located below the surface of the impact, but throughout the region of the impact as shown in Figure 3.7(c). Similar to the strain distributions, the stress distributions also showed the maximum stresses throughout the region of the impact, however, in contrast to both the strain and stress distributions, high strain-rate distributions were observed throughout the brain tissue (Figure 3.8(c)). As expected, for an impact depth of 0.35 mm (Figure 3.7(a)), the maximum strain values predicted by the FE model were less than the baseline case, but the peak strain-rate values were the same as the baseline case and are seen distributed on the surface of the cortex, at the impact site (Figure 3.8(a)).

Similar to the strain distribution contours for an impact depth of 0.3 mm, decreasing the velocity to 2.35 m/s showed peak mechanical responses less than the baseline

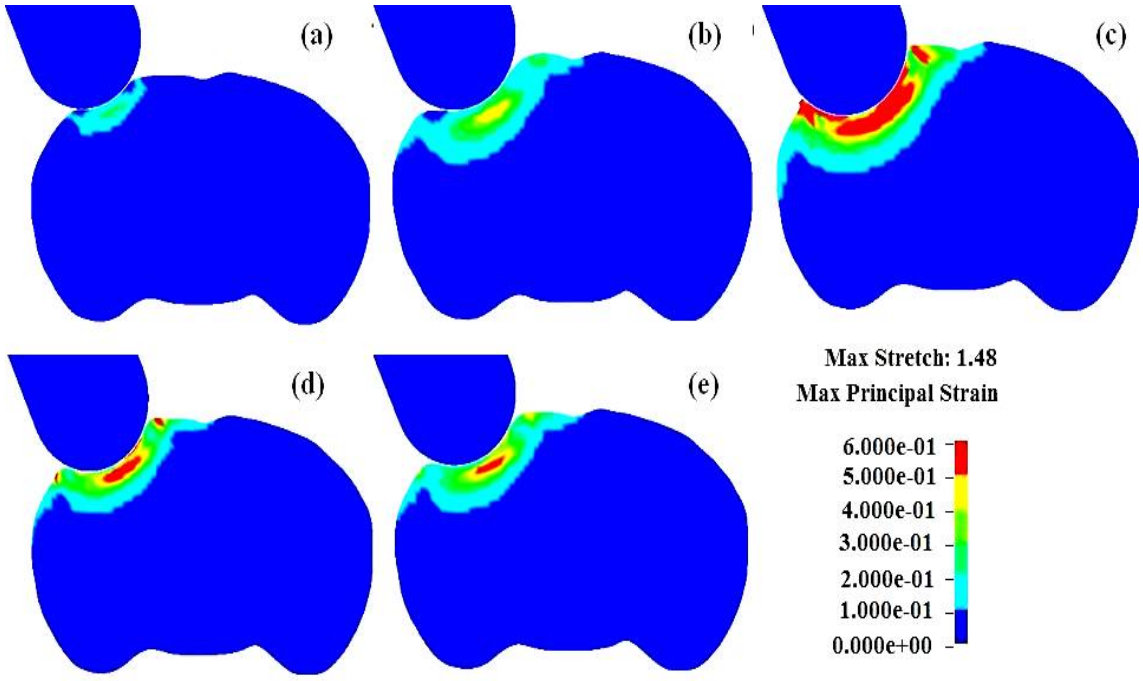

Figure 3.7. Green-Lagrange first principal strain distribution on a coronal section of the brain tissue, at the center of the impact site for a maximum depth and velocity of (a) 0.35 mm and 4.7 m/s, (b) 0.7 mm and 2.35 m/s, (c) 1.05 mm and 4.7 m/s, (d) 0.7 mm and 7.05 m/s, (e) baseline Case (0.7 mm and 4.7 m/s).

case (Figure 3.7(b)). However, increasing the velocity to 7.05 m/s showed maximum strains higher than the baseline case, and these maximum strains were observed below the surface of the impact same as in the baseline case. Figures 3.10 and 3.11 show the maximum strain and stress values in the brain tissue at the site of the impact as a function of impact depth and velocity, listed in Table 2.2 . From Figures 3.10 and 3.11 it can be seen that decreasing the depth to 0.35 mm resulted in a decrease of peak strain by 52.3 % and a decrease of peak stress by 18 %, compared to the baseline case depth of 0.7 mm, while increasing the depth to 1.05 mm produced an increase in strains by 71.4 % and stress by 14.4 %. Furthermore, decreasing the velocity of the impact to 2.35 m/s led to a decrease of 28.5 % in the strain and 43.3 % in the stress, while increasing the velocity of the impact to 7.05 m/s led to an increase of 38 % in strains and 42.1 % in stresses, compared to the baseline case velocity of 4.7 m/s. The results from the parameter study suggest that the depth of impact had the

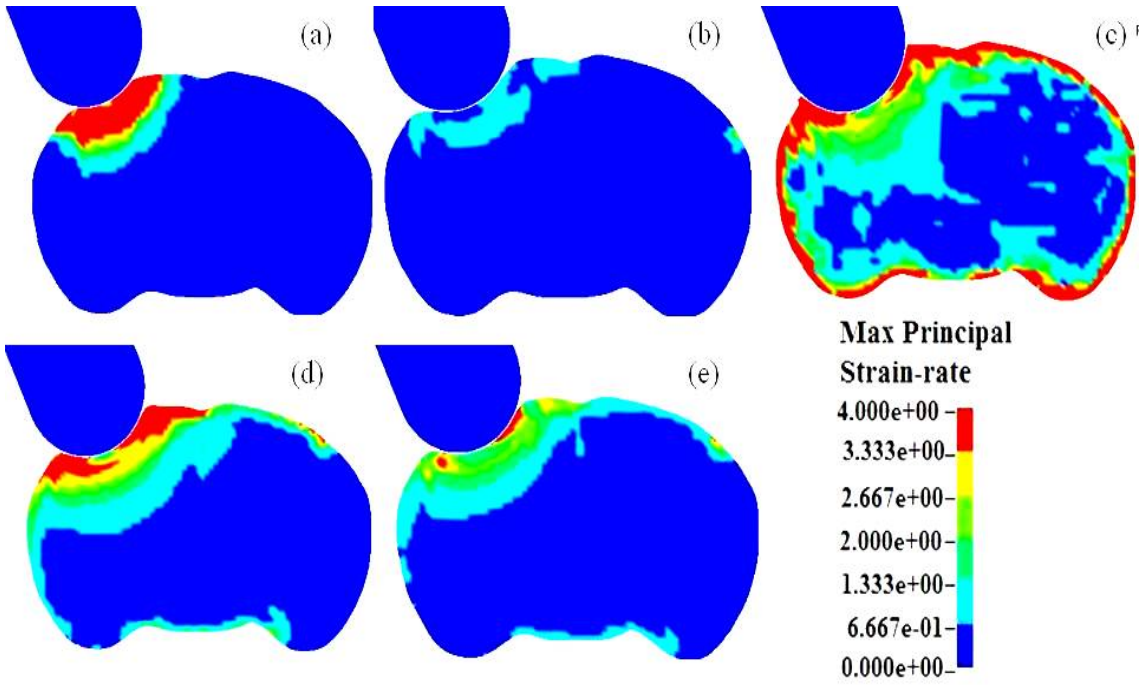

Figure 3.8. Logarithmic first principal strain-rate distribution on a coronal section of the brain, at the center of the impact site for a maximum depth and velocity of (a) 0.35 mm and 4.7 m/s, (b) 0.7 mm and 2.35 m/s, (c) 1.05 mm and 4.7 m/s, (d) 0.7 mm and 7.05 m/s, (e) baseline case (0.7 mm and 4.7 m/s). Units: ms^{-1}

largest influence on the strains, while the velocity of impact had the largest influence on the stresses.

3.1.2 Mesh convergence

The mesh convergence study was performed as shown in Table 2.3, by increasing the number of elements until convergence was attained. Varying the element size of the brain tissue each time while keeping the element size constant for the other layers in the realistic model resulted in intersections and penetrations between the elements of different layers, and hence was not done. However, changing the element size in all the layers of the realistic model and then defining the loading parameters accordingly did not have the same problem definition, hence attaining a perfect convergence was difficult. Due to the above explained intricacies, an idealized model was used as the basis to test for the convergence. The idealized model built by extruding the elements

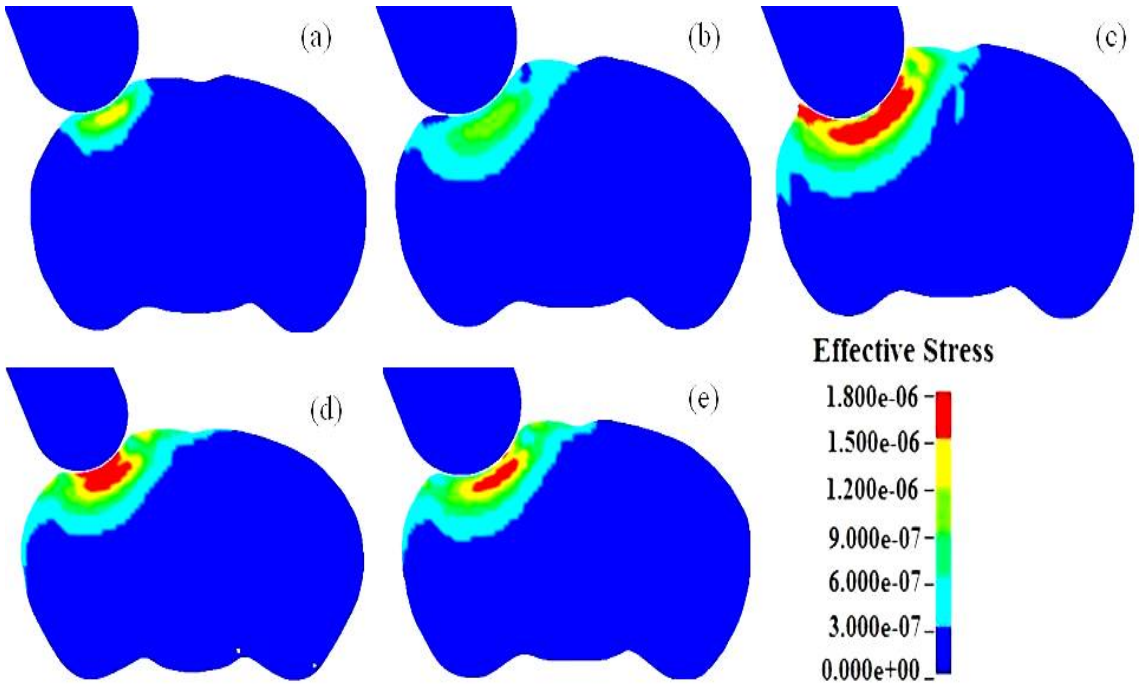

Figure 3.9. Effective stress distribution on a coronal section of the brain, at the center of the impact site for a maximum depth and velocity of (a) 0.35 mm and 4.7 m/s, (b) 0.7 mm and 2.35 m/s, (c) 1.05 mm and 4.7 m/s, (d) 0.7 mm and 7.05 m/s, (e) baseline case (0.7 mm and 4.7 m/s). Units: GPa

of a coronal section had less complexity, and thus only the element size for the brain tissue and the pia-arachnoid were varied until the convergence was attained.

Three regions of interest, one at the center of the impact and two at the boundary of the craniotomy, were selected to check for convergence. Baseline loading conditions and material parameters were used, with the Green-Lagrange first principal strain as the outcome measure. Figure 3.12 shows the Green-Lagrange first principal strain on the brain tissue plotted against element size at the regions of interest. As shown in Figure 3.12, the maximum strain remained constant at all three regions of interest for element sizes of 110 μm and above, indicating convergence. As the mesh was dependent on geometry, the element size of 110 μm would not have the same number of elements in the realistic model as in the idealized model. In order to translate results from the idealized simulation into the realistic model, the mesh density in the craniotomy area in the idealized case was used as the basis for meshing the realistic model. Therefore, the mesh density around the hole in the idealized model had 801

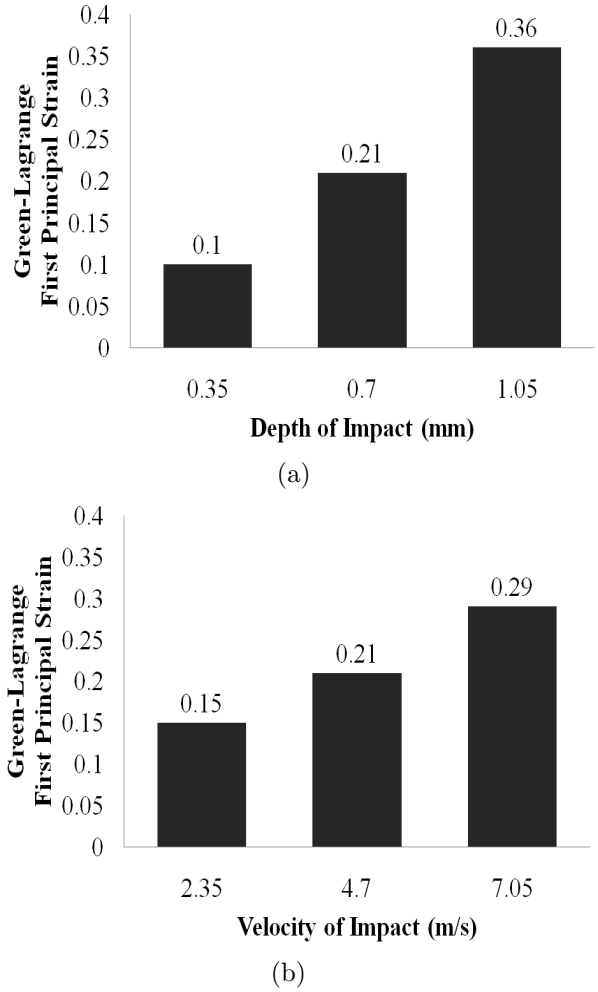

Figure 3.10. Green-Lagrange peak first principal strain in the brain at the site of the impact due to change in (a) the depth, and (b) velocity of the impact.

elements at the site of the impact, while the realistic model meshed with an element size of 117 μm had 832 elements in the region, greater than the idealized model. Any number of elements above 801 would be acceptable as the solution converged with 801 element and hence the brain tissue, meshed with an element size of 117 μm was appropriate for predicting the mechanical responses accurately.

3.1.3 Study of impactor geometry and size

Influence of shape and size of the impactor was studied under three different scenarios in comparison to the baseline simulation. The strain distributions in the

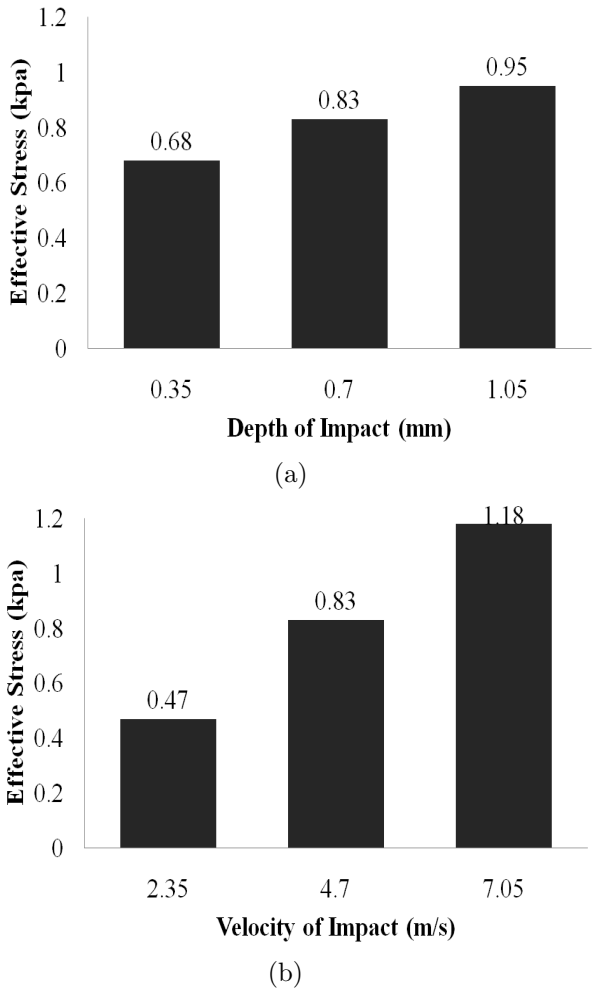

Figure 3.11. Effective stress in the brain at the site of the impact due to change in (a) the depth, and (b) velocity of the impact.

brain tissue from all three simulations, as shown in the Figure 3.13, were plotted to understand the influence of shape and size in comparison to the baseline case. In Figures 3.13(a) and 3.13(b), the strain distributions due to a flat impactor tip show maximum strains on the brain tissue in and around the site of the impact. The elements on the brain tissue at the surface of the impact experienced the largest deformations, and a very high strain value of 0.61 was recorded on those elements, compared to 0.21 recorded in the baseline case. Unlike the baseline case, where the peak strains were located below the impact surface (Figure 3.2(b)), the peak strains with a flat impactor tip occurred on the cortical surface (Figure 3.13(a)). However, the

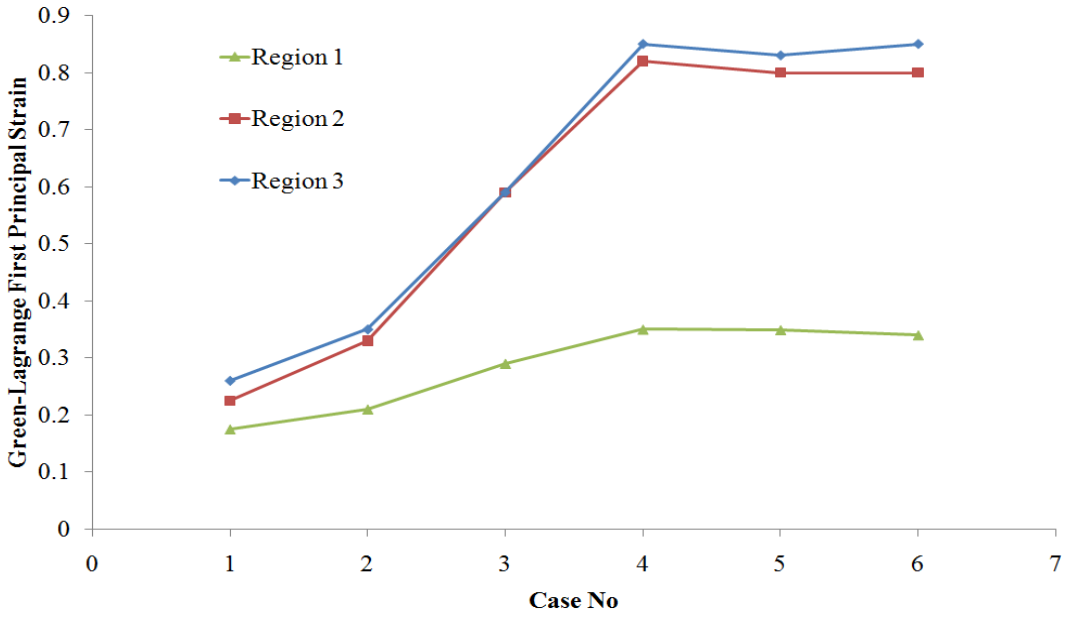

Figure 3.12. Green-Lagrange first principal strain as a function of case no. (element size in Table 2.3), plotted for the idealized model.

maximum strains were surprisingly also observed below the cortical surface (Figure 3.13(a)) but adjacent to the impact site rather than at its center.

Figures 3.13(c) and 3.13(d) show the strain distributions with a semi-flat impactor tip at a maximum depth of 0.7 mm. Similar to the strain distributions shown in Figures 3.13(a) and 3.13(b), the maximum strains with the semiflat impactor were observed around the perimeter of the impact (Figure 3.13(d)). Even with a semi-flat impactor the maximum strains were seen below the cortical surface (Figure 3.13(d)), but adjacent to the impact site. Unlike the maximum strains observed below the surface of the impact in the baseline case (Figure 3.2(b) at the center of the impact, the maximum strains with a semi-flat impactor tip were concentrated only on the cortical layers (Figure 3.13(d)). The maximum strain value recorded with the semi-flat impactor for the elements at the site of impact was higher (0.56) than the baseline case (0.21) but less compared to the flat impactor tip (0.61). The results from the above simulations show that shape of the impactor had a significant influence on the mechanical responses predicted. Both the flat and the semi-flat impactor shapes produced much higher strains when compared to the hemispherical tip, and the sharp ends of the impactors appear to induce these high strains. Use of these different

impactor shapes in the animal experiments might lead to different types and extents of injury.

In contrast to impactor shape, changing the impactor diameter did not have a dramatic infulence on outcomes. The strain distributions produced by a large diameter impactor (Figure 3.13(e) and 3.13(f)) produced results similar to the baseline case. The maximum strains were seen below the surface of the impact (Figure 3.13(e)) and no strains were observed away from the site of the impact (Figure 3.13(f)). However, the maximum strain value recorded for the brain tissue was 0.84, higher than that of the baseline case (0.67). This increase in strains was expected due to the increase in the volume of the impactor, resulting in larger contact forces.

3.1.4 Dwell time study

The effect of dwell time was studied in two simulations, by holding the impactor at its maximum impact depth for 0.5 and 1 ms. Figure 3.14 shows the Green-Lagrange first principal strain plots for 0 (baseline), 0.5, and 1 ms dwell time. During the dwell time period, no further deformations in the brain tissue were observed than those induced at the time of the impact. As shown in the Figure 3.14, during the dwell time period, 0.15 - 0.65 ms in a 0.5 ms dwell time case and 0.15 - 1.15 in a 1 ms dwell time case, the rate of release in the strains was less than the baseline case. It can be observed that increasing the dwell time period further decreased the rate of release in the strains thereby causing the strains to remain constant for the remaining time of impactor's contact with the brain tissue. However, once the impactor started its return to its original position, further decrease in strains was observed. In experimental CCI models, the dwell time typically used ($\sim$ 100 ms) is much longer than those used in this study; such a long dwell time was not simulated here due to computational expense. However, the results from the shorter time suggest that larger dwell times would only result in a longer times of slowly decreasing strain in the strain time-history plots. The effect of dwell time on injury is not clear.

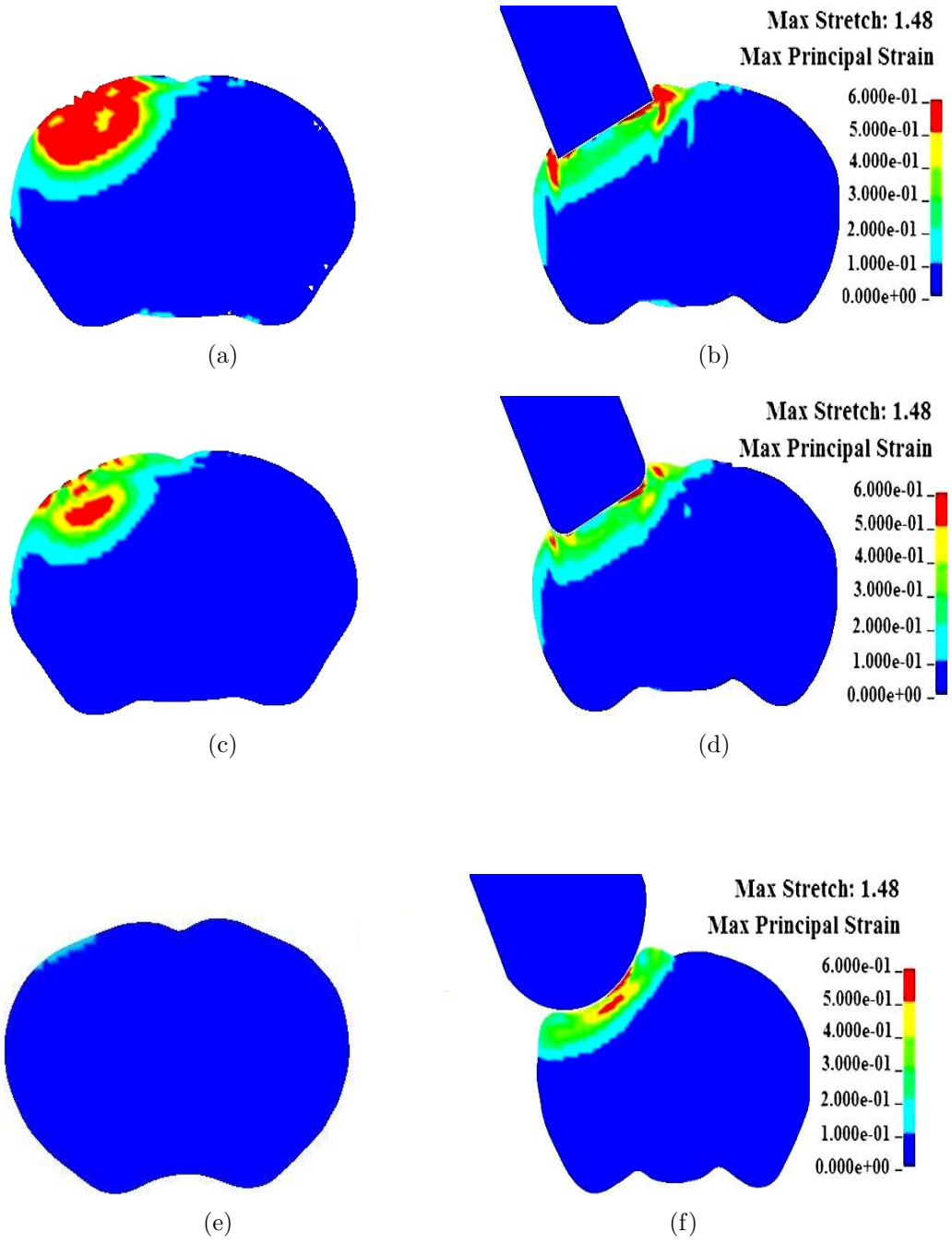

Figure 3.13. Green-Lagrange first principal strain distribution on a coronal section of the brain tissue, adjacent to the impact site with a (a) flat impactor, (c) semi-flat impactor, and (e) larger diameter impactor, and at the center of the impact site with a (b) flat impactor, (d) semi-flat impactor, and (f) larger diameter impactor, for a maximum depth of 0.7 mm.

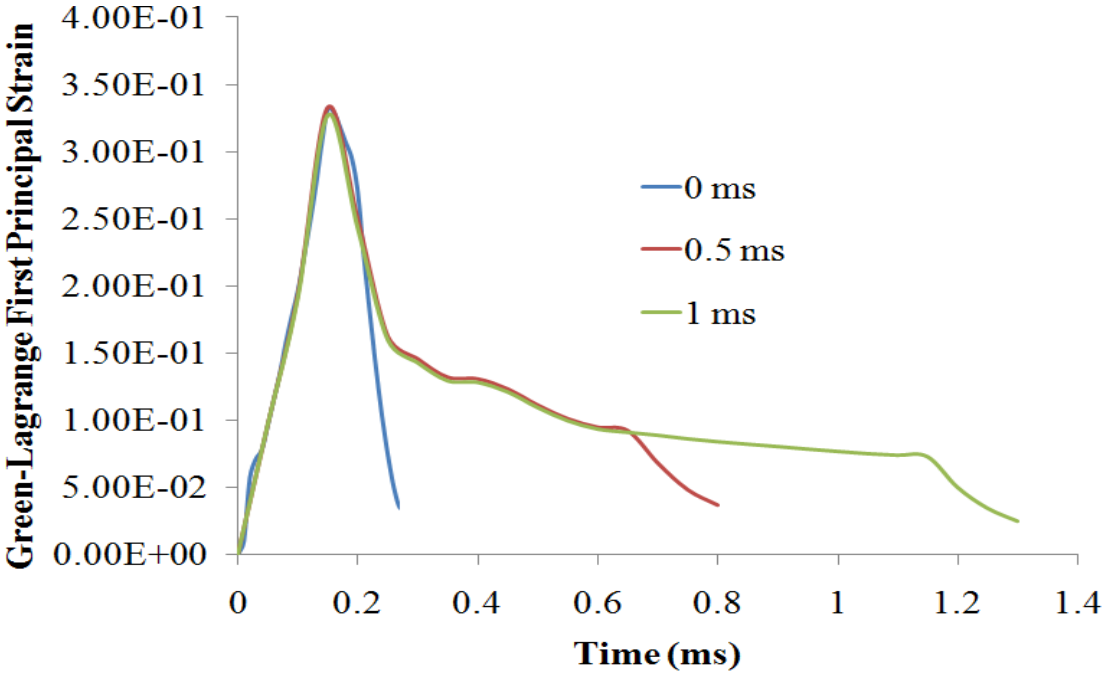

Figure 3.14. Green-Lagrange first principal strain plotted over time for the elements on the brain tissue with a 0 (baseline), 0.5 and 1 ms dwell time.

3.1.5 Material parameter study

In this study, the decay constant (β), which governs a viscoelastic material's transition from viscous to elastic response, and the short-term shear modulus (G_0) were changed to study their influence on the mechanical responses. The baseline case decay constant of 20 ms was changed to 5 and 40 ms for comparison. However, the decay constant did not seem to influence the FE model predicted strain responses. The maximum predicted strain was 0.657 with a 5 ms decay constant at 0.15 ms, and was 0.672 with a 40 ms decay constant. The strain values are less than 2 % different (Figure 3.15) from the baseline case maximum strain value of 0.67. These results correlate with findings by Mao et al. [23], which also showed the similar small differences in strain values compared to the baseline case (20 msec). However, unlike the strains, the stress responses were different compared to the baseline case responses (Figure 3.16) . The maximum effective stress for a simulation with a 5 ms decay constant at 0.15 ms was notably greater (2.86 kPa) than that of the baseline (1.83 kPa) case. Increasing the decay constant to 40 ms decreased the effective stress from 1.83 to 1.45 kPa.

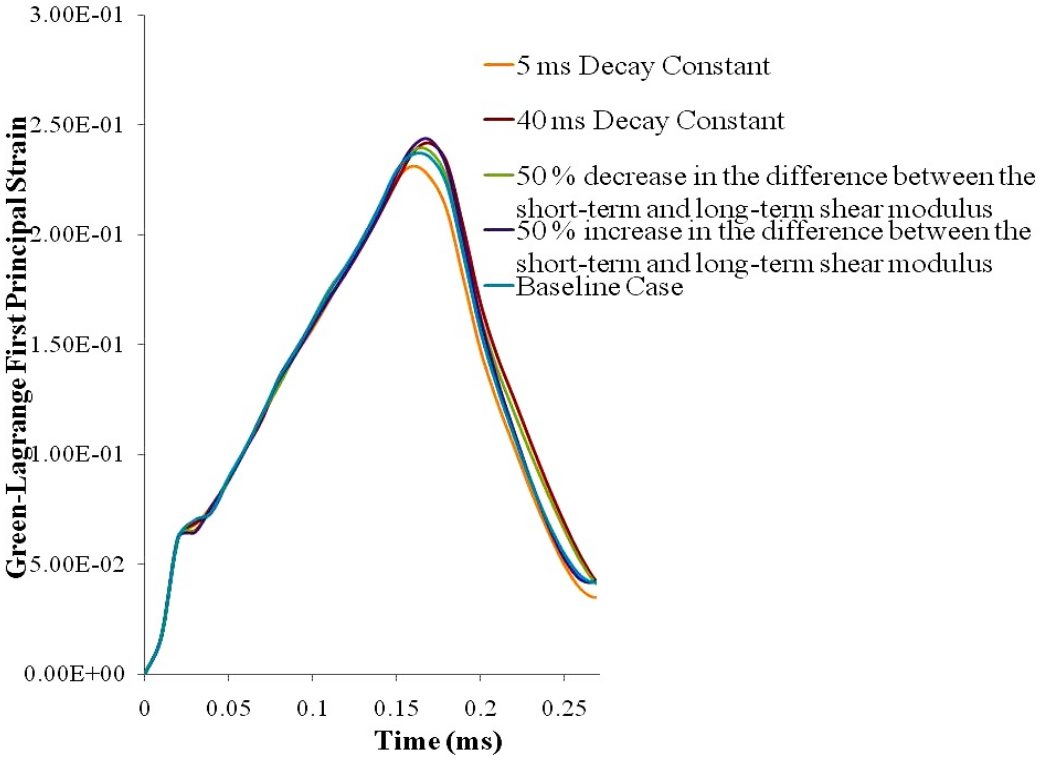

Figure 3.15. Green-Lagrange first principal strain over time for different, decay constants and short-term shear modulus.

Two simulations were run to examine the effect of shear relaxation modulus (G(t)) by changing the short-term shear modulus (G_0) such that the difference between the long-term (G_∞) and the short-term shear modulus (G_0) was increased and decreased by 50% in comparision to the baseline case. In both simulations, responses similar to those of the decay constant study were observed. The percentage difference in the maximum strain values was less than 2 % (Figure 3.15) of the baseline case; an increase in stress (2.18 kPa) was observed with G_0= 2.32 kPa, while decreased stress (1.45 kPa) resulted for G_0= 1.11 kPa compared to the baseline case stress value (1.83 kPa).

In addition to the above simulations, a material model study was conducted by modeling the brain tissue as linear elastic. The elastic material parameters for the brain tissue (E= 66.7 KPa and ν= 0.49) were taken from the literature [29], and the density of the material was kept the same as the baseline. In contrast to the viscoelastic case, elements at the center of the impact site in the elastic case showed

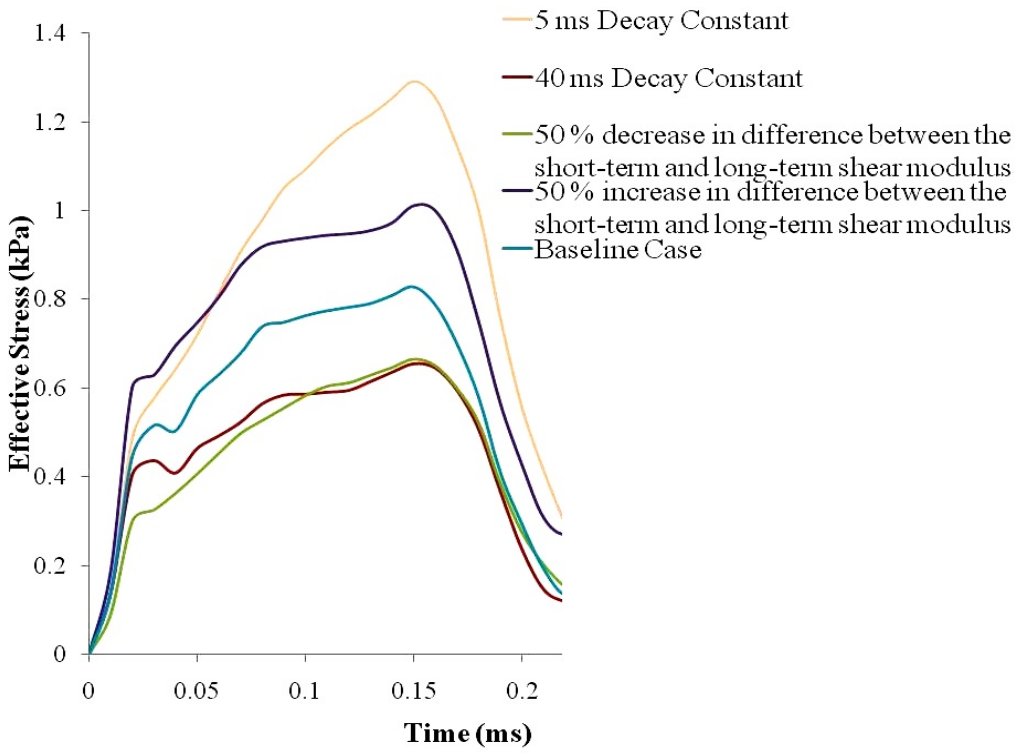

Figure 3.16. Effective stress plotted over time for different decay constants and short-term shear modulus.

maximum strain (Figure 3.17) before the impactor reaches its maximum depth. This behavior in the strain plot suggests no further deformation of the brain tissue after the initial impact. In the elastic material model simulation, peak strains were predicted to be only below the surface of the impact as observed in the viscoelastic case, and the strains at the surface of the impact were notably lower than the baseline case. A maximum strain value of 0.59, 12 % less than the baseline case value of 0.67, was recorded in the brain tissue below the surface of the impact at the time the impactor was at its maximum depth (Figure 3.18). The maximum stress recorded in the brain tissue with the elastic material model was 50.7 kPa, which is much higher than that of the baseline case, 1.8 kPa. The high predicted stress was due to much higher stiffness of the brain tissue in this case. Since, the magnitude of material stiffness used in both the material models differ largely, a qualitative comparison between the results was studied, but for a quantitative comparison material parameters more closely relating to each other are to be taken into consideration.

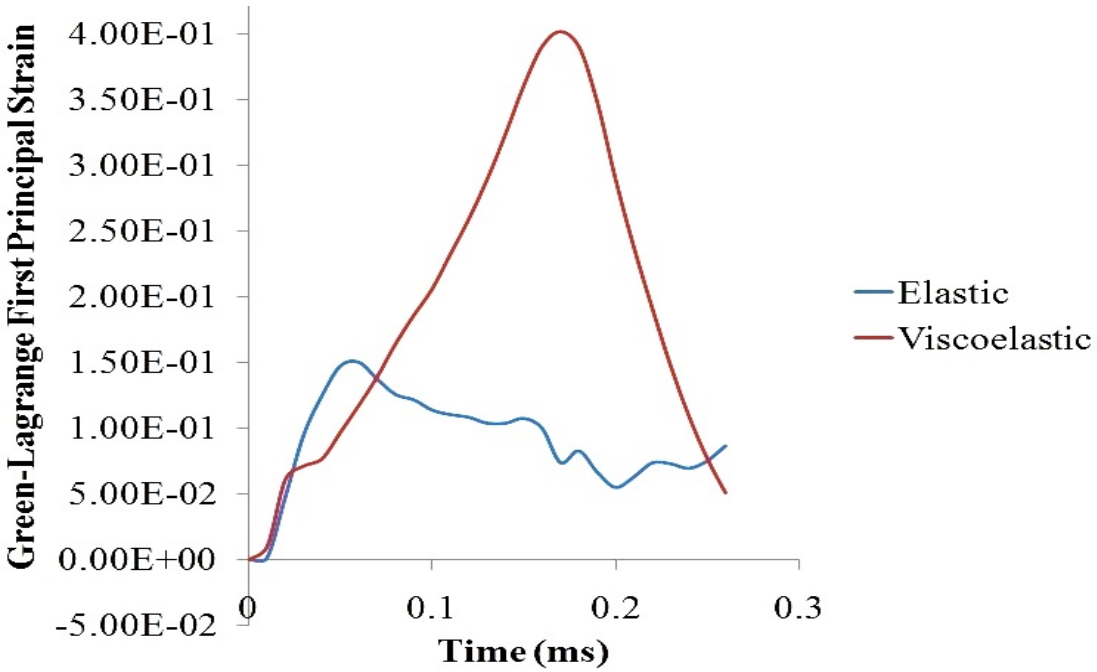

Figure 3.17. Comparison of elastic and viscoelastic material model strain plots for the elements on the brain tissue at the center of the impact site.

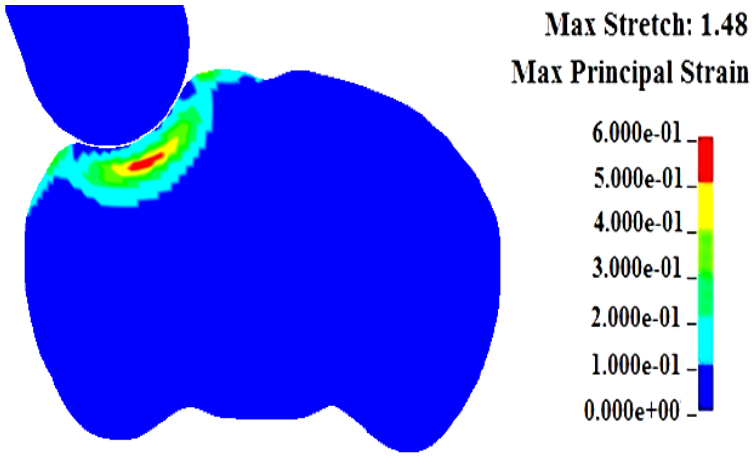

Figure 3.18. Green-Lagrange first principal strain distribution contour in a elastic material model for a maximum depth of 0.7 mm.

3.1.6 Site of impact

The influence on mechanical responses due to change in the impact site was studied by positioning the impactor at 2.7 mm posterior of the bregma and 1 mm lateral of the sagittal suture on the left hemisphere. The brain tissue, the meninges, and the skull were rotated to an angle of 20°, such that the impactor was perpendicular to the surface of the dura. The change in impact site showed a peak strain value of 0.62 in comparison to the baseline case value of 0.67, a percentage difference of 7.4%. As with the baseline case, maximum strain (Figure 3.19) occurred below the impact surface.

3.1.7 Influence of craniotomy size and foramen magnum

3.1.7.1 Craniotomy size

In all the presented CCI simulations the diameter of the hole (craniotomy size) was approximately 3.5 mm, while the baseline impact depth was 0.7 mm. At the time of the impact, the brain tissue was observed to extrude out through the craniotomy, around the impactor (Figure 3.20), due to its incompressibility, and as a result, the elements on the brain tissue around the site of the impact (periphery of the impactor) were severely distorted. It was not clear whether the extrusion of brain tissue observed in the FE model would occur in the CCI animal experiments, and

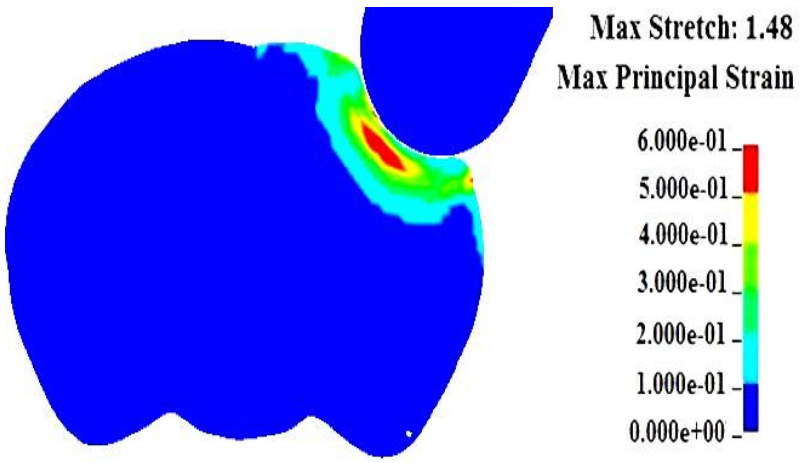

Figure 3.19. Green-Lagrange first principal strain distribution contour for a simulation with change in impact site for a maximum depth of 0.7 mm.

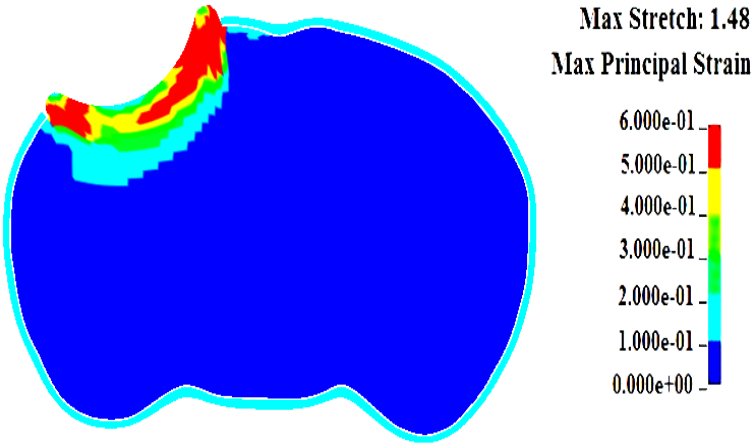

Figure 3.20. Green-Lagrange first principal strain distribution on a coronal section of the brain tissue at the center of the impact site for a maximum depth of 0.7 mm, in a simulation without any gap between the meninges.

therefore, high-speed camera was used to capture the deformation of the brain tissue for an experiment conducted on a mice cadaver. As shown in Figure 3.21, no extrusion of the brain tissue was observed in the CCI experiments and therefore, to avoid the extrusion in the FE model, a small gap of 0.01 mm was introduced between the dura and the pia-arachnoid. However, an alternative of using a larger diameter craniotomy was also considered as a possible solution. As expected, with a larger craniotomy (Figure 3.22), the brain tissue had more space around the impactor to deform. This space created due to a larger diameter hole decreased the chances of extrusion of the brain and reduced the distortion of elements.

3.1.7.2 Foramen magnum

This study did not account for the foramen magnum nor other internal and surrounding structures of the brain tissue. However, we looked at the influence of incorporating the foramen magnum into the FE model by creating a small hole on the caudal side of the skull. Without accounting for the spinal cord, however, it was not clear how to most accurately model its influence. In addition to just removing the skull elements, an alternative was explored where the dura and pia-arachnoid elements around the hole were also removed from the model. Baseline loading conditions and

Figure 3.21. CCI experiment image showing the deformation of the brain tissue (with skull and dura intact).

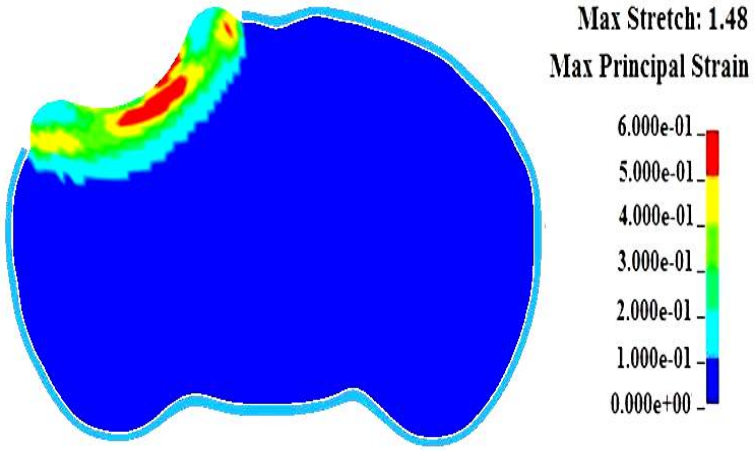

Figure 3.22. Green-Lagrange first principal strain distribution on a coronal section of the brain tissue at the center of the impact site for a maximum depth of 0.7 mm, in a simulation with a larger diameter of the hole.

material parameters were used in this study and the gap between the meninges was removed.

As shown in Figure 3.23, the brain tissue was seen extruded out through the foramen magnum when none of the meninges were included at the foramen magnum. Momentum gained by the tissue led to continued brain tissue extrusion even after the impactor was released. As a result, strains around the foramen magnum were excessive. At the site of the impact, however, the peak strains observed were in the same range as those observed in the other CCI simulations presented. As expected, this approach alleviated excessive extrusion of the brain tissue between the skull and impactor, but it is not likely that such large displacements occur at the foramen mangnum. While it may be helpful to model displacements at the foramen magnum, a more realistic approach is recommended.

3.1.8 Comparison between the idealized and the realistic model

Figure 3.24 shows the stress distributions in the brain tissue for the idealized model with baseline loading conditions and material parameters. Similar to the realistic model, the maximum stresses were observed below the surface of the impact and on the surface. The peak stresses in the idealized mouse brain were recorded when the

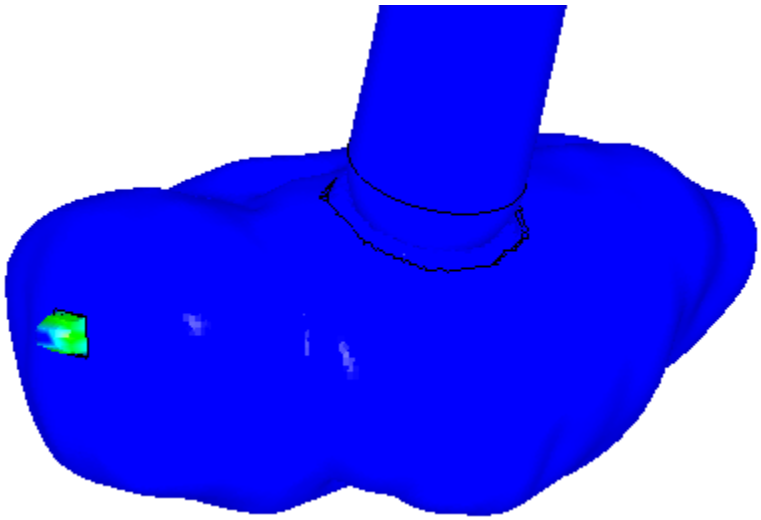

Figure 3.23. Deformation of the brain tissue in the presence of foramen magnum (with skull and meninges removed around the hole).

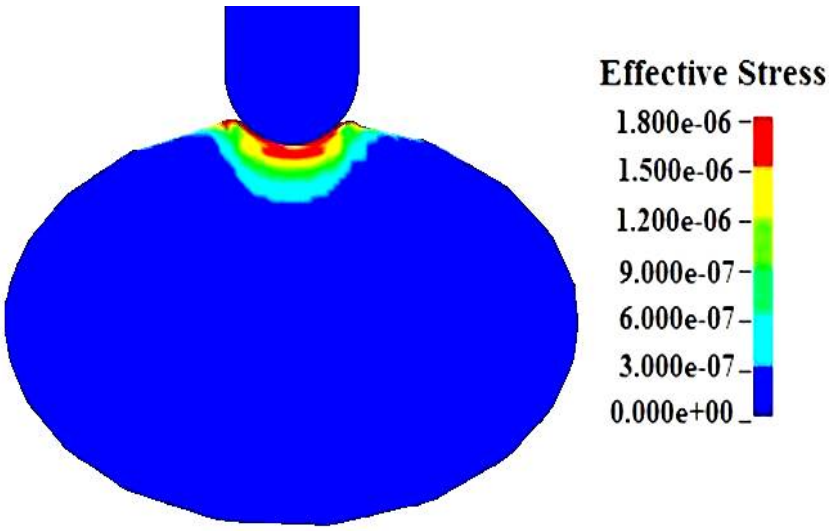

Figure 3.24. Effective stress distribution in the idealized model, for a maximum depth of 0.7 mm. (Stress units in GPa)

impactor was at its maximum depth. Surprisingly, the strain distributions on the idealized brain tissue (Figure 3.25) show maximum strains at the impact surface, and not below as in all the realistic model simulations. However, similar to the baseline case, all the peak mechanical responses in the idealized model were localized at the site of the impact.

These results clearly show the influence of geometry on the mechanical responses predicted by the both the models. Even though few similarities in the distribution of peak mechanical responses is visible, this idealized model might be misleading in predicting thresholds for injury.

3.2 Discussion

In this study, the surface geometry of the mouse brain, and its anatomical relations with the surroundings (as observed within a head) were modeled. In doing this, certain techniques like introducing the gap between the meninges, modeling the dura and skull separately, etc. had to be followed to represent the model as close to reality as possible. This model was later simulated over a range of loading conditions as described in section 2.5. This section presents a brief discussion in relation to

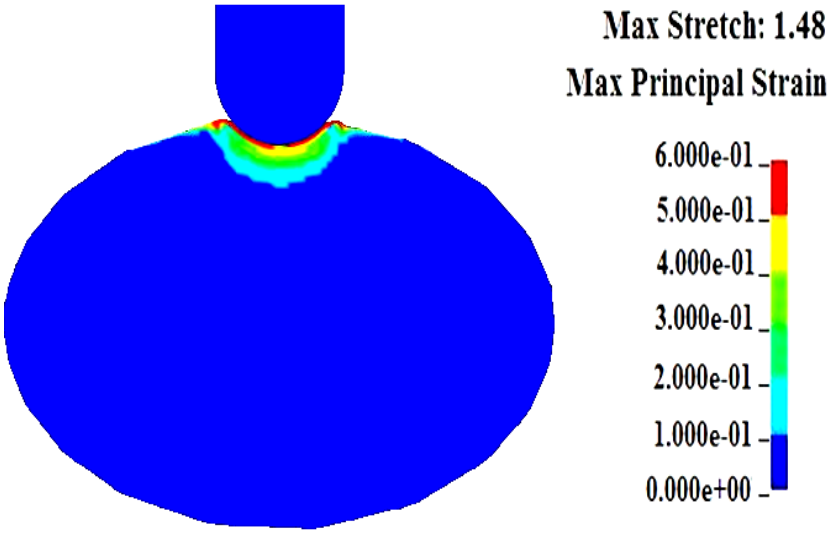

Figure 3.25. Green-Lagrange first principal strain distribution in the idealized model, for a maximum depth of 0.7 mm.

these above mentioned techniques and the results from the various loading conditions simulated.

3.2.1 Gap between the dura and pia-arachnoid

In all the presented CCI simulations, a gap of 0.01 mm was introduced between the dura and the pia-arachnoid layer. Initially, in the FE model the brain was packed tightly within the skull, resulting in the extrusion of the brain tissue through the hole (craniotomy) during the impact. This led to the unrealistic distortion of the brain tissue elements around the periphery of the impactor, so the gap was introduced to reduce the distortion. In the current FE model, neither the brain stem nor the foramen magnum were modeled. Ventricles were also not accounted for. Incorporating these features into the model might have made it less likely that the brain tissue would have extruded, thus negating the need for the gap. Moreover, in this model, the pia and the arachnoid layer were modelled as one single layer, but in reality they are separated by the subarachnoid space, filled with cerebrospinal fluid. Since, these structures were not accounted for in the model, due to lack of data, introducing the gap was considered the best choice.

3.2.2 Contact interactions

Contact interactions were assigned between both the dura and the pia/arachnoid and the dura and the skull. In reality the dura is firmly attached to the skull. The dura was thus modeled with shell elements on the inner surface of the skull, such that the inner surface of the skull and the dura shared nodes. However, this approach was not successful, because the dura would not deform except in the region of the craniotomy. This approach did not allow dura near the craniotomy to separate from the skull during the impactor penetration and, as a result, led to severe dural distortion within the craniotomy. It was thus determined that skull and the dura should be modeled separately with an automatic surface to surface algorithm defining contact between them. The pia-arachnoid shared common nodes with the brain tissue outer surface and therefore a contact interaction was not assigned between the two.

3.2.3 Results

The effect of various external parameters like the impact depth and velocity, the shape and size of the impactor, and the site of the impact were studied using the current FE model of the mouse brain. It can be deduced from Figure 3.26 that impactor shape had the most significant influence on the FE model predicted strain responses, atleast over the variable ranges considered. Both alternative impactor shapes, flat and semiflat, used for this study showed much higher strains in comparison to the baseline case than any other external parameter variation. The high strains observed with the different impactor shapes were the result of brain tissue being compressed only in the impact direction. This deformation of the brain tissue in the impact direction led to the elements on the brain tissue around the impactors periphery to be stretched rapidly resulting in severe deformations. The leading edges of these impactor shapes are expected to be the reason for these deformations. However, the baseline impactor did not have such response because of its spherical end, compressing the dura, allowed the deformation of the elements on the brain tissue around the impactors periphery to be distributed radially. Impactor depth had the second highest influence on the strain responses. As the penetration depth increased, the brain tissue was naturally stretched further, leading to high strains in the region

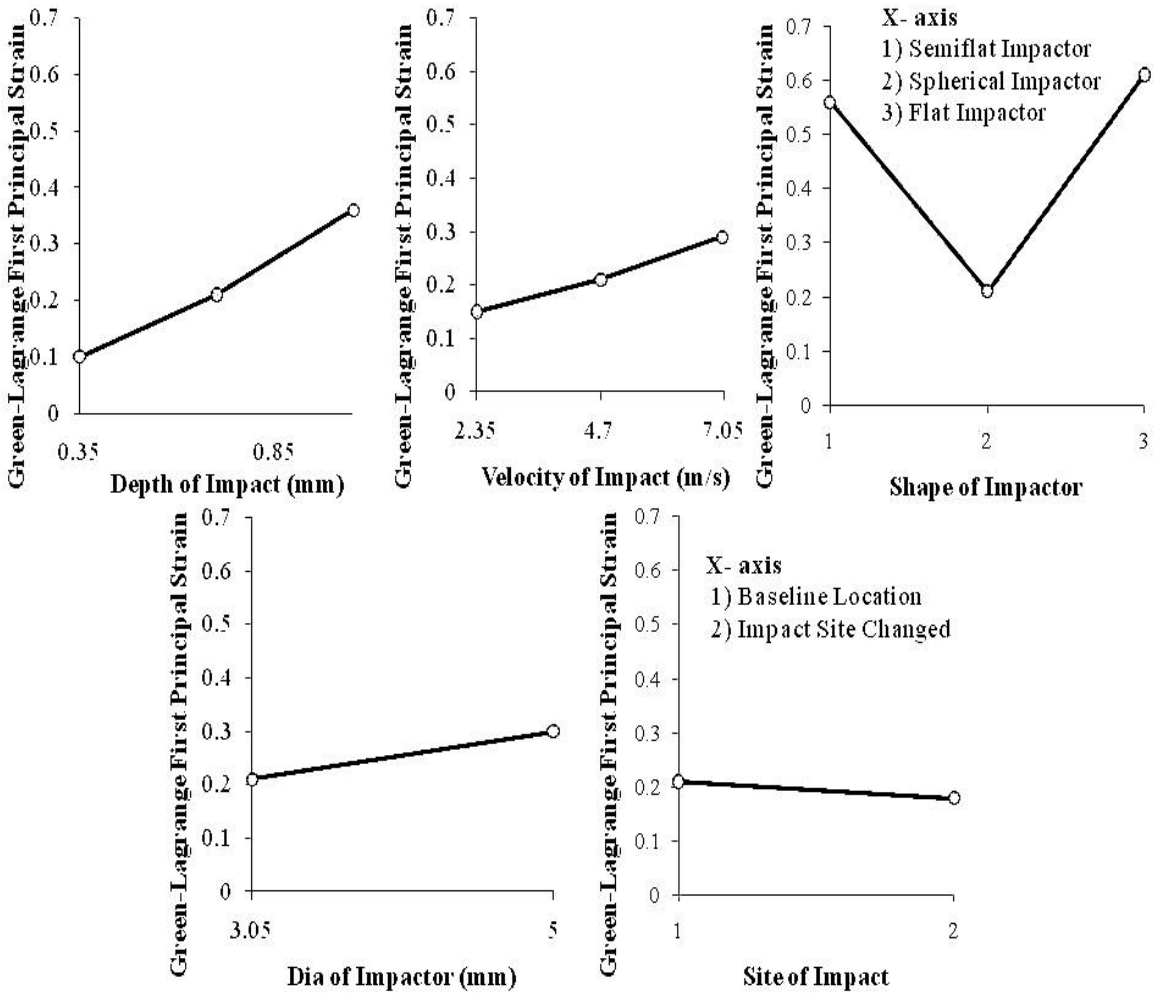

Figure 3.26. The effect of external parameters influencing the FE model predicted strain responses.

of the impact. The change in the impactor size and the velocity of the impact had less influence than shape of the impactor and depth of impact. Furthermore, site of impact had negligible influence on the strain values. Similar to the results presented by Mao et al. [22], impact velocity and size of the impactor were shown to have little influence on strain. The study by Mao et al. [22], however, showed impact depth to be leading factor and shape of the impactor to be the next leading factor influencing the model predicted mechanical responses. Impact depths simulated in their study were much higher than in this study; this likely explains the difference in findings.

Moreover, the baseline impactor used in their study was a semiflat impactor and not a spherical one, which could also be a reason for difference in the results.

Not surprisingly, the study on dwell time showed that holding the impactor at its maximum depth resulted in a constant strain in the model for the time the impactor is held in its position. However, the consequences of dwell time on injuries needs to be investigated by conducting experiments with and without the dwell time on the animal models. In the material parameters study it was observed that increasing the decay constant to 40 ms resulted in lower peak stress and also a shift in the release of stresses in the stress time-history plot shown in Figure 3.16, compared to the smaller decay constants (5 and 20 ms). This change in peak stress and the rate of release in stresses was expected because the higher decay constant results in a faster decay time, leading to a faster transition from the viscous to elastic response. Similarly, decreasing the decay constant leads to a much higher time for the transition between the viscous and elastic response. Also, increasing the difference between the long-term and short-term shear modulus meant that the model had higher instantaneous shear modulus (viscous stiffness) and a slower release of stresses. Decreasing the difference between the two led to a decrease in the instantaneous modulus and a faster release of stresses, as observed in Figure 3.16.

In the elastic material model study, the occurrence of peak stresses below the surface of impact correlates with the study by Heinrich Hertz on the stress distributions in elastic solids [25]. Additionally, it was observed that the elastic material model undergoes more displacement than the visocelastic material model as shown in Figure 3.27. In the elastic material model, once the impactor was released there is an increase in the area of brain tissue, which undergoes displacement. This displacement observed in the elastic material model is expected due to the elasticity of the model, releasing strains more rapidly, while the viscoelastic material model has a slow rate of release in strains due to its viscous nature and therefore not much displacement is expected in this case.

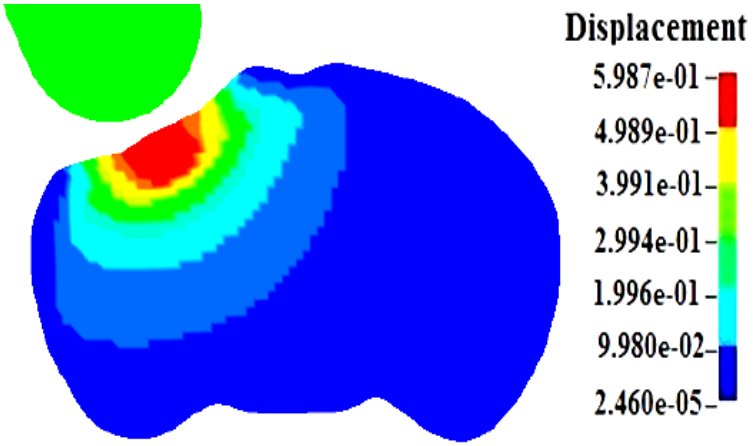

(a)

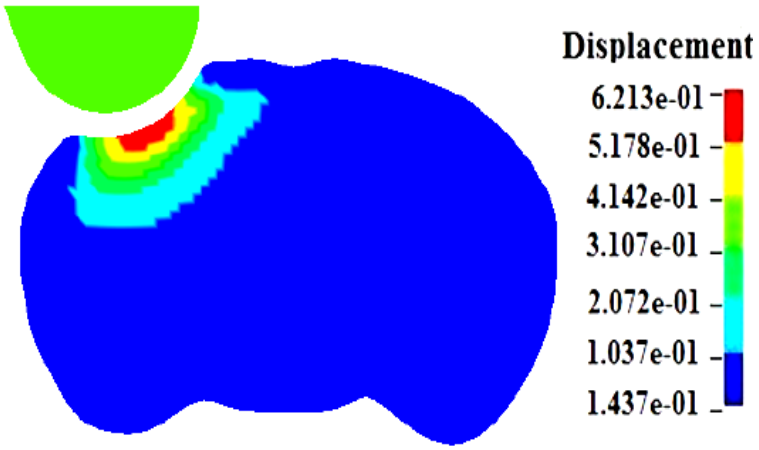

(b)

Figure 3.27. The resultant displacement distribution (mm) on the brain tissue in (a) elastic and (b) viscoelastic material models after impactor release.

CHAPTER 4

CONCLUSIONS AND FUTURE WORK

This chapter includes the conclusions drawn from the CCI simulations and also presents the future scope for the model.

4.1 Conclusions

- A 3D FE model of CCI in a mouse was built to quantify the deformations associated with the resulting contusion.
- This FE model predicted the impactor shape and depth to be the most influential parameters affecting the mechanical responses, while the impact site and the diameter of the impactor were the least influential parameters.
- The use of dwell time showed no change in the mechanical response for the period the impactor was in contact with the brain tissue.
- As expected, an increase in short-term shear modulus led to a delay in the release of stresses, while decrease in the shear modulus led to faster release of stresses.
- The peak mechanical responses for both the elastic and viscoelastic material model were observed below the surface of the impact.
- Introducing foramen magnum into the model showed a drastic difference in the deformation of the brain tissue, however, without accounting for spinal cord, incorporating foramen magnum might be misleading.
- The correlation of the obtained mechanical responses with experimental injuries will be studied to predict the thresholds for injuries.

4.2 Future Work

As observed in all the presented CCI results, the deformations predicted by the FE model were not compared with any experimentally observed injuries, due to the lack of data. However, future work involves the comparison of model predictions with experimental injury to study correlation between mechanical response and injury. Moreover, this research focused on predicting the deformations of homogeneous brain tissue. However, the cortex and underlying white matter tracts include a dense network of blood vessels. Incorporating this vasculature in the brain tissue of the current FE model, at least to some extent, could be important in more accurately predicting thresholds for contusion injury.

This research should also be further extended to include a more detailed geometry including the internal structures of the brain tissue, which were refrained from this study. As shown in Section 4.1, the incorporation of foramen magnum influenced the predicted deformations severely, but only incorporating foramen magnum and neighbouring spinal cord may be an important addition in a future model. The interaction of brain tissue with its surroundings (the skull and the meninges) should also be represented more accurately by more accurately modeling the structure of the meninges and the inner skull.

The brain tissue in this study was modeled as linear viscoelastic and homogeneous. In reality the brain is an inhomogeneous material so modeling the brain as a inhomogenous model with distinct gray and white matter properties should also be taken into consideration. Furthermore, in the literature the brain tissue is also been modeled as linear elastic and in some cases as a nonlinear viscoelastic. It is recommended that brain tissue material properties be further investigated by conducting experiments to accurately identify an appropriate material model for computational studies. Lastly, the validation of the FE model with the experimental stress and strain data is needed to improve the biofidelity of the model.

APPENDIX

FINITE ELEMENT CODE

This chapter presents the reduced FE code generated using HyperMesh for controlled cortical impact baseline simulation presented in the previous chapters.

```
$$ Ls-dyna Input Deck Generated by HyperMesh Version  : 10.0build60
$$ Generated using HyperMesh-Ls-dyna 971 Template Version : 10.0build60

$---+----1----+----2----+----3----+----4----+----5----+----6----+----7----+----8
*KEYWORD  50000000

Units: mm, kg, ms, kN, GPa
$---+----1----+----2----+----3----+----4----+----5----+----6----+----7----+----8
*CONTROL_TERMINATION
$$  ENDTIM    ENDCYC     DTMIN    ENDENG    ENDMAS
       0.3

*CONTROL_TIMESTEP
$$  DTINIT    TSSFAC      ISDO    TSLIMT     DT2MS      LCTM     ERODE     MSIST
                0.4

*CONTROL_BULK_VISCOSITY
$$      Q1        Q2        IBQ
       1.5      0.06         1

*CONTROL_ENERGY
$$    HGEN      RWEN    SLNTEN     RYLEN
         2
$---+----1----+----2----+----3----+----4----+----5----+----6----+----7----+----8

DATABASE_OPTION -- Control Cards for ASCII output

$---+----1----+----2----+----3----+----4----+----5----+----6----+----7----+----8

*DATABASE_ELOUT
      0.03         0

*DATABASE_GLSTAT
      0.03         0

*DATABASE_MATSUM
      0.03         0

*DATABASE_BINARY_D3PLOT
$$ DT/CYCL      LCDT      BEAM     NPLTC
```

```
      0.01
         0

*DATABASE_EXTENT_BINARY
$$   NEIPH     NEIPS    MAXINT    STRFLG    SIGFLG    EPSFLG    RLTFLG    ENGFLG
                                        1         1
$$  CMPFLG    IEVERP    BEAMIP     DCOMP      SHGE     STSSZ    N3THDT    IALEMAT
                                                                      2
$$ NINTSLD   PKP_SEN      SCLP               MSSCL     THERM

$---+----1----+----2----+----3----+----4----+----5----+----6----+----7----+----8

Define Nodes

$---+----1----+----2----+----3----+----4----+----5----+----6----+----7----+----8

*NODE
   node               x               y               z


$---+----1----+----2----+----3----+----4----+----5----+----6----+----7----+----8

Define Parts and Materials

$---+----1----+----2----+----3----+----4----+----5----+----6----+----7----+----8

$$$$ Material Properties

*MAT_ELASTIC
$HMNAME MATS       Dura Material Properties
        mid        ro         e        pr
         2     1.1300E-06    0.0315   0.45
*MAT_ELASTIC
$HMNAME MATS       Pia-arachnoid Material Properties
        mid        ro         e        pr
         3    1.1300E-06    0.0125    0.45
*MAT_RIGID
$HMNAME MATS       Rigid Material Properties (Skull and Impactor)
       mid        ro         e        pr
        4    7.8500E-06     200.0    0.28

*MAT_KELVIN-MAXWELL_VISCOELASTIC
$HMNAME MATS       Brain Material Properties
       mid        ro           K
        1    1.0400E-06       2.1  1.7200E-06  5.1000E-07      20.0   1.0

$$$$$ Part Id's

*PART
$HMNAME COMPS       Pia-arachnoid
$HWCOLOR COMPS       2       3
        pid       sid       mid     eosid      hgid      grav    adpopt

         2         2         3
```

```
$HMNAME COMPS       Dura
$HWCOLOR COMPS       3      61
        pid       sid       mid     eosid      hgid      grav    adpopt

         3         1         2
$HMNAME COMPS       Skull
$HWCOLOR COMPS       4      53
        pid       sid       mid     eosid      hgid      grav    adpopt

         4         3         4
$HMNAME COMPS       Brain
$HWCOLOR COMPS       5      58
        pid       sid       mid     eosid      hgid      grav    adpopt

         5         3         1
$HMNAME COMPS       Impactor
$HWCOLOR COMPS       6      22
        pid       sid       mid     eosid      hgid      grav    adpopt

         6         3         4

$$$$$ Section Properties

*SECTION_SHELL
$HMNAME PROPS       Shell(Dura)
       sid    elform      shrf       nip     propt   qr/irid     icomp
         1         1                    0                 0.0
        t1        t2        t3        t4      nloc
      0.02      0.02      0.02      0.02       0.0

*SECTION_SHELL
$HMNAME PROPS       Shell (Pia-arachnoid)
        sid    elform      shrf       nip     propt   qr/irid     icomp
         2         1                    0                 0.0
        t1        t2        t3        t4      nloc
     0.015     0.015     0.015     0.015       0.0

*SECTION_SOLID
$HMNAME PROPS       Solid(Skull,brain and impactor)
        sid    elform
         3        1

$---+----1----+----2----+----3----+----4----+----5----+----6----+----7----+----8

Define loading conditions and contact interactions

$---+----1----+----2----+----3----+----4----+----5----+----6----+----7----+----8

*BOUNDARY_PRESCRIBED_MOTION_RIGID
$HMNAME LOADCOLS       Impactor Motion
$HWCOLOR LOADCOLS       1       7
       pid        dof       vad      lcid
         6         2         2         1
```

```
*BOUNDARY_SPC_NODE
$HMNAME LOADCOLS       Constraints
$HWCOLOR LOADCOLS       2       3
       nid       cid      dofx      dofy      dofz     dofrx     dofry     dofrz
   2035907         0         1         0         1         1         1         1
   2009365         0         1         1         1         1         1         1

*DEFINE_CURVE (LCID)
           1
          0.0               0.0
         0.15               0.7
         0.30               0.0


*CONTACT_AUTOMATIC_SURFACE_TO_SURFACE_ID
$HMNAME GROUPS       Skull and dura
$HWCOLOR GROUPS       1       3
         1
         3         4         3         3
       0.2       0.2

         1


*CONTACT_AUTOMATIC_SURFACE_TO_SURFACE_ID
$HMNAME GROUPS      Dura and pia-archnoid
$HWCOLOR GROUPS       2       4
         2
         2         3         3         3
       0.2       0.2

         2


*CONTACT_AUTOMATIC_SURFACE_TO_SURFACE_ID
$HMNAME GROUPS       Dura and piston
$HWCOLOR GROUPS       3       5
         3
         3         6         3         3
       0.2       0.2

         2

$---+----1----+----2----+----3----+----4----+----5----+----6----+----7----+----8

Define Elements

$---+----1----+----2----+----3----+----4----+----5----+----6----+----7----+----8

*ELEMENT_SHELL
      eid     pid      n1      n2      n3      n4


*ELEMENT_SOLID
```

```
      eid     pid      n1      n2      n3      n4    n5      n6      n7      n8
*END
```

REFERENCES

[1] "AmScien Instruments." http://www.amscien.com//.

[2] A. Marmarou, M. A. A.-E. Foda, W. van den Brink, J. Campbell, H. Kita, and K. Demetriadou, "A new model of diffuse brain injury in rats part i: Pathophysiology and biomechanics," *Journal of Neurosurgery*, vol. 80, no. 2, pp. 291–300, 1994.

[3] G. D. Rosen, A. G. Williams, J. A. Capra, M. T. Connolly, B. Cruz, L. Lu, D. C. Airey, K. Kulkarni, and R. W. Williams, ""The Mouse Brain Library @ www.mbl.org"." http://www.mbl.org/atlas170/atlas170_frame.html//, 2000. Int Mouse Genome Conference 14: 166.

[4] H. Mao, L. Zhang, K. H. Yang, and A. I. King, "Application of a finite element model of the brain to study traumatic brain injury mechanisms in the rat," *Stapp Car Crash Journal*, vol. 50, pp. 583–600, November 2006.

[5] M. Faul, X. L, W. MM, and C. VG, "Traumatic brain injury in the United States: Emergency Department Visits,Hospitalizations and Deaths 2002-2006," (Atlanta), Centers for Disease Control and Prevention,National Center for Injury Control and Prevention, 2010.

[6] J.W.Finnie, "Animal models of traumatic brain injury: a review," *Australian Veterinary Journal*, vol. 79, pp. 628–633, September 2001.

[7] J.W.Finnie and P.C.Blumbergs, "Traumatic brain injury," *Veterinary Pathology*, vol. 39, pp. 679–689, November 2002.

[8] I. Cernak, "Animal models of head trauma," *NeuroRx*, vol. 2, pp. 410–422, July 2005.

[9] A. I. King, K. H. Yang, L. Zhang, and W. Hardy, "Is head injury caused by linear or angular accelration?," in *IRCOBI Conference Proceedings*, September 2003.

[10] H. Mao, *Computational Analysis of In Vivo Brain Trauma*. PhD thesis, Wayne State University, 2009.

[11] D.M.Morales, N.Marklund, D.Lebold, H.J.Thompson, A.Pitkanen, W.L.Maxwell, L.Longhi, H.Laurer, M.Maegele, E.Neugebauer, D.I.Graham, N.Stocchetti, and T.K.McIntosh, "Experimental models of traumatic brain injury: Do we really need to build a better mousetrap," *Neuroscience*, vol. 136, pp. 971–989, 2005.

[12] J. W.Lighthall, C. Dixon, and T. E.Anderson, "Experimental models of brain injury," *Journal of Neurotrauma*, vol. 6, November 1989.

[13] J. W.Lighthall, "Controlled cortical impact: A new experimental brain injury model," *Journal of Neurotrauma*, vol. 5, 1988.

[14] C. Dixon, G. L.Clifton, J. W.Lighthall, A. A.Yaghmai, and R. L.Hayes, "A controlled cortical impact model of traumatic brain injury in the rat," *Journal of Neuroscience Methods*, vol. 39, pp. 253–262, 1991.

[15] M. B.Potts, H. Adwanikar, and L. J.Noble-Haeusslein, "Models of traumatic cerebellar injury," *Cerebellum*, vol. 8, pp. 211–221, 2009.

[16] Y. Tang, Y. Noda, T. Hasegawa, and T. Nabeshima, "A concussive-like brain injury model in mice (ii): selective neuronal loss in the cortex and hippocampus," *Journal of Neurotrauma*, vol. 14, pp. 863–873, November 1997.

[17] Y. Shapira, E. Shohami, A. Sidi, D. Soffer, S. Freeman, and S. Cotev, "Experimental closed head injury in rats: Mechanical pathophysiologic and neurologic properties," *Critical Care Medical*, vol. 16, pp. 258–265, 1988.

[18] T. Gennarelli, L. Thibault, J. Adams, D. Graham, C. Thompson, and R. Marcincin, "Diffuse axonal injury and traumatic coman in the primate," *Annals of neurology*, vol. 12, pp. 564–574, 1982.

[19] A.Pena, J.D.Pickard, D.Stiller, N.G.Harris, and M.U.Schuhmann, "Brain tissue biomechanics in cortical contusion injury:a finite element analysis," *Acta Neurochirurgica*, vol. 95, pp. 333–336, 2005.

[20] A. Levchakov, E. Linder-Ganz, R. Raghupathi, S. S. Margulies, and A. Gefen, "Computational studies of strain exposures in neonate and mature rat brains during closed head impact," *Journal of Neurotrauma*.

[21] D. I.Shreiber, A. C.Bain, and D. F.Meaney, "In vivo thresholds for mechanical injury to the blood-brain barrier," *Society of Automotive Engineers*, 1997.

[22] H. Mao, K. H. Yang, A. I. King, and K. Yang, "Computational neurotrauma-design,simulation,and analysis of controlled cortical impact model," *Biomechanics and Modeling in Mechanobiology*, 2010.

[23] H. Mao, X. Jin, L. Zhang, K. H. Yang, T. Igarashi, L. J. Noble-Haeusslein, and A. I.King, "Finite element analysis of controlled cortical impact-induced cell loss," *Journal of Neurotrauma*, vol. 27, pp. 877–888, May 2010.

[24] M. Shafieian, K. K.Darvish, and J. R.Stone, "Changes to the viscoelastic properties of the brain tissue after traumatic axonal injury," *Journal of Biomechanics*, vol. 42, pp. 2136–2142, 2009.

[25] K.L.Johnson, *Contact Mechanics*. Cambridge University Press, 1985.

[26] Livermore Software Technology Corporation, Livermore,CA, *LS-DYNA Theoretical Manual*, May 1998.

[27] "Kxcad." http://www.kxcad.net/ansys/ANSYS/ansyshelp/Hlp_L_hour1.html//.

[28] E. G. Takhounts, R. H. Eppinger, J. Q. Campbell, R. E. Tannous, E. D. Power, and L. S. Shook, "On the development of the simon finite element head model," *Stapp Car Crash Journal*, vol. 47, pp. 107–133, October 2003.

[29] J. Galford and J. McElhaney, "A viscoelastic study of scalp, brain, and dura," *Journal of Biomechanics*, p. 211221, 1970.